Earth and Planetary Science Letters 288 (2009) 335–347

Contents lists available at ScienceDirect

Earth and Planetary Science Letters

journal homepage: www.elsevier.com/locate/epsl

An experimental study of pyroxenite partial melts at 1 and 1.5 GPa: Implications for the major-element composition of Mid-Ocean Ridge Basalts

Sarah Lambart *, Didier Laporte, Pierre Schiano

Laboratoire Magmas et Volcans, Université Blaise Pascal - CNRS - IRD, 5 rue Kessler, F-63038 Clermont-Ferrand Cedex, France

ARTICLE INFO

Article history:
Received 20 July 2009
Received in revised form 21 September 2009
Accepted 25 September 2009
Available online 17 October 2009

Editor: L. Stixrude

Keywords:
experimental petrology
pyroxenite
partial melting
primitive MORB

ABSTRACT

To better assess the potential role of pyroxenites in basalt generation at mid-ocean ridges, we performed partial melting experiments on two natural websterites and one clinopyroxenite representative of worldwide pyroxenites. The experiments were conducted at 1 and 1.5 GPa in a piston-cylinder apparatus; the microdike technique was used to separate the liquid from the solid phases and to obtain reliable glass analyses even at low degrees of melting. Contrasted melting behaviors were observed depending on the phase proportions at the solidus, especially the abundance of orthopyroxene. (1) If orthopyroxene is abundant, the main melting reaction is similar to the melting reaction in peridotites (clinopyroxene + orthopyroxene ± spinel = liquid + olivine), and the liquids are similar to peridotite-derived melts for most major elements. (2) In the absence of orthopyroxene, the main melting reaction is clinopyroxene + spinel = liquid + olivine, yielding liquids that are strongly depleted in SiO_2 in comparison to peridotite-derived melts. This low-SiO_2 content can be associated with a high FeO content, a combination usually ascribed to a high average pressure of melting (of a peridotitic source).
Because of their higher melt productivities and lower solidus temperatures, 5 wt.% of pyroxenites in a heterogeneous mantle may contribute up to 40 wt.% of the total melt production. (1) In some cases, pyroxenite-derived melts differ strongly from peridotite partial melts, leading to a distinct pyroxenite signature in the average melt (lower alkali and TiO_2 contents, lower SiO_2, higher FeO and/or lower Mg#). The classical criteria used to select primitive mantle-derived magmas (melt inclusions hosted into high Mg# olivine or MORB glasses with Mg# ≥67) or to track down enriched mantle sources (MORB glasses with high incompatible element contents) must be considered with caution, otherwise melts carrying a pyroxenite signature may be eliminated. (2) In general, however, the major-element signature of pyroxenites should be hardly detectable in the average melt because of the similarity of most pyroxenite-derived melts with peridotite partial melts. This similarity may explain why MORB have relatively uniform major-element compositions, but may have variable trace element and/or isotopic compositions.

1. Introduction

The main mechanism involved in the generation of Mid-Ocean Ridge Basalt (MORB), the most voluminous rock type on the Earth's surface, is polybaric partial melting of the lherzolitic mantle ascending beneath mid-ocean spreading centers. Assuming a homogeneous mantle, the major-element variability of MORB is generally explained in terms of variations of the potential temperature of the ascending mantle (Klein and Langmuir, 1987; McKenzie and Bickle, 1988; Langmuir et al., 1992) and low-pressure fractionation (Grove et al., 1992). There are, however, several aspects of MORB composition, including variations in abundance of trace elements (e.g., Allègre et al., 1995; Niu and Batiza, 1997), in volatile and halogen contents (e.g., Michael and Schilling, 1989; Michael, 1995) and in isotope ratios (e.g., Dupré and Allègre, 1983; Blichert-Toft et al., 1999; Eiler et al., 2000) that cannot easily be explained in the case of a homogeneous source. Moreover several lines of evidence indicate that the mantle contains a significant fraction of pyroxenites (Schulze, 1989), which present a large spectrum of bulk-rock composition (Fig. 1) and modal proportions, and which may play an important role in controlling the chemical variability of mantle-derived melts (Sleep, 1984; Allègre and Turcotte, 1986; Sobolev et al., 2007). At last models based on trace elements and isotopic systematics (e.g., Hirschmann and Stolper, 1996) have emphasized the role of pyroxenites in MORB generation. Accordingly, one may wonder why pyroxenites would control isotopic and trace element systematics of MORB without significantly affecting their major-element compositions.

High-pressure experiments on a range of pyroxenite bulk compositions have allowed us to better constrain the melting relations of these rocks at pressure P higher than 2 GPa, and their role in the generation of oceanic island basalts (e.g., Yasuda et al.,

* Corresponding author. Clermont Université, Université Blaise Pascal, Laboratoire Magmas et Volcans, BP 10448, F-63000 Clermont-Ferrand. Tel.: +33 4 73 34 67 21; fax: +33 4 73 34 67 44.
E-mail address: S.Lambart@opgc.univ-bpclermont.fr (S. Lambart).

0012-821X/$ – see front matter © 2009 Elsevier B.V. All rights reserved.
doi:10.1016/j.epsl.2009.09.038

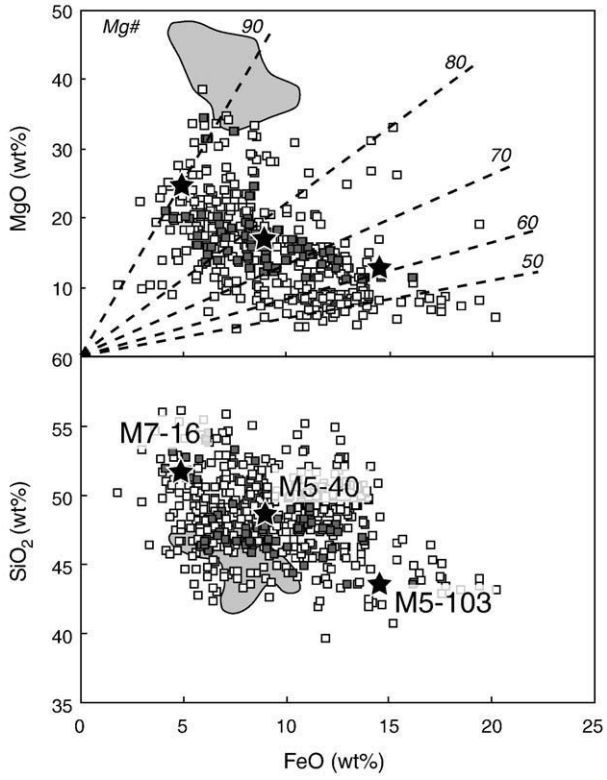

Fig. 1. Plots of MgO and SiO_2 vs. FeO for natural pyroxenites (small squares; pyroxenites from the Beni Bousera ultramafic massif are shown by the small grey squares); the stars are starting materials M5–103, M5–40 and M7–16. The grey area is the mantle peridotite field from GEOROC database (http://georoc.mpch-mainz.gwdg.de). The pyroxenite data come from compilation of Hirschmann and Stolper (1996) completed with analyses from Becker (1996), Bodinier et al. (2008), Dessai et al. (2004), Dickey (1970), Ducea (2002), Garrido and Bodinier (1999), Ghent et al. (1980), Jahn et al. (2003), Kornprobst (1970), Kumar et al. (1996), Kuno and Aoki (1970), Lee et al. (2006), Liu et al. (2005), Melcher et al. (2002), Porreca et al. (2006), Santos et al. (2002), Schmickler et al. (2004), Tang et al. (2007), Volkova et al. (2004), and Xu (2002).

1994; Kogiso et al., 1998; Hirschmann et al., 2003; Pertermann and Hirschmann, 2003b; Keshav et al., 2004; Kogiso and Hirschmann, 2006). Assuming a normal oceanic crust thickness (7 ± 1 km), most petrologic models (e.g., Langmuir et al., 1992; Kinzler and Grove, 1992) predict a mean pressure of melting less than 1.5 GPa (for peridotitic mantle). To constrain the role of pyroxenites on the major-element compositions of primitive MORB, it is therefore necessary to compare melt compositions and degrees of melting in peridotites and pyroxenites at $P<2$ GPa. At present, very little is known about the melting behavior of pyroxenites at $P<2$ GPa. Ito and Kennedy (1974) realized melting experiments on a pyroxenite between 1 atm and 2.5 GPa. However, they used Pt capsules without inner graphite container and so their charges may have suffered iron loss. Adam et al. (1992) investigated partial melting of two garnet pyroxenites at 1.3–2 GPa, but the presence of some water in their experiments led to the crystallization of amphibole.

We have selected three natural pyroxenites that cover the composition ranges of natural pyroxenites (Fig. 1), and we have determined experimentally their melting relations and phase compositions at 1 and 1.5 GPa. Although this contribution is primarily focused on intermediate to large degrees of melting, we also analysed liquid compositions at low degrees of melting, down to 2.6%. Comparing our data with previous studies on the peridotitic system (Hirose and Kushiro, 1993; Baker and Stolper, 1994; Baker et al., 1995; Kushiro, 1996; Robinson et al., 1998; Falloon and Danyushevsky, 2000; Wasylenki et al., 2003; Laporte et al., 2004), (1) we try to find discriminating features between pyroxenite-derived and peridotite-derived melts, and (2) we discuss the relative contributions of pyroxenites and peridotites to basalt generation and the influence of pyroxenite-derived melts on the major-element composition of MORB. This work provides the first experimental study of the influence of pyroxenite on the major-element compositions of MORB. Moreover, it extends the database of pyroxenite partial melts from the literature, in which compositions at low degrees of melting were almost completely lacking up to now.

2. Experimental and analytical procedure

2.1. Selection of starting materials

In order to select representative compositions of pyroxenites, a principal component analysis was first performed on normalized major-element compositions of a worldwide pyroxenite dataset from the literature (see references in Fig. 1 caption). This technique gives the principal directions of the data cloud, expressed mathematically by the eigenvectors of the variance–covariance matrix of the data, and the associated principal variances, which are the corresponding eigenvalues. Three natural pyroxenites from the Beni Bousera ultramafic massif were selected to account for the dispersion of the data (Fig. 1). Sample M5–40 is a garnet websterite, which plots very close to the mean of the pyroxenite population. It contains 16.6 wt.% MgO, and its Mg# [that is, the molar ratio $100 \times Mg^{2+}/(Mg^{2+}+Fe^{2+})$] is equal to 76.7 (Table 1). The two other samples plot on the opposite sides of the first principal component axis, which expresses the largest linear dispersion of the data. Sample M5–103 is an olivine websterite with 24.6 wt.% MgO and Mg# = 89.8; compared with M5–40, it is enriched in SiO_2, and depleted in Al_2O_3, FeO, TiO_2, and Na_2O. Sample M7–16 is a garnet–olivine clinopyroxenite, with 12.5 wt.% MgO and a low Mg# (60.6); compared with M5–40, it is depleted in SiO_2 and Na_2O, and enriched in FeO, CaO, and TiO_2. The three pyroxenites are olivine (Ol) normative, but show different degrees of silica undersaturation: M7–16 is nepheline (Ne) normative (2.3%), M5–40 is hyperstene (Hy) normative (8.3%), and M5–103 is strongly Hy-normative (31.3%).

2.2. Experimental and analytical techniques

Pyroxenites were crushed in an agate mortar, and ground under ethanol to 2–4 μm using an agate micronizing mill. They were then fired for 6 h at 900 °C in a CO_2/H_2 atmosphere with an oxygen fugacity between the magnetite–wüstite and the iron–wüstite buffers ($f_{O2} = 10^{-15.91}$ bar). All powders were stored under vacuum to minimize the adsorption of water. The experiments were made in a non-end-loaded, 3/4-inch piston-cylinder apparatus, using double containers made of graphite and platinum; containers, assemblages, and experimental techniques are similar to those described in Lambart et al. (2009).

To analyse the composition of liquids in equilibrium with mineral phases, we used the "microdike" technique (Laporte et al., 2004). In all the experiments, we observed a few microdikes (Fig. 2), both at the top and at the bottom of the graphite sample chamber, which vary from tens to hundreds of microns in length and from a few microns to hundreds of microns in width. Degrees of melting (from 2.6 to 95.0 wt.%) and run durations in our study (Table 2) are such that the liquid in the microdikes is in equilibrium with neighboring mineral phases (Laporte et al., 2004). Moreover, Lambart et al. (2009) showed that the average glass compositions measured at the top and at the bottom of the sample chamber are equal within error in a given experiment, indicating thus a small temperature gradient (~5 °C) in the sample chamber.

At the end of an experiment, the capsule was enclosed in epoxy, sectioned lengthwise, polished and carbon-coated. Textures, phase assemblages (Table 2) and compositions (Table 1) were characterized using a JEOL JSM-5910 LV scanning electron microscope and a Cameca SX100 electron microprobe. A 15-kV accelerating voltage, a 15-nA

Table 1
Compositions (wt.%) of starting materials M5–103, M5–40 and M7–16, and average compositions of liquid in partial melting experiments.[a]

Run no.	Ph	SiO_2	TiO_2	Al_2O_3	Cr_2O_3	FeO	MnO	MgO	CaO	Na_2O	K_2O	Total	Mg#[b]	Ne/Ol/Hy/Di/Fds[c]
M5–103		51.64	0.09	7.17	0.60	4.97	0.10	24.57	10.13	0.71	0.02		89.8	0/18/31/27/22
M5–40		48.53	0.52	12.37	0.12	9.02	0.20	16.64	10.89	1.65	0.06		76.7	0/28/8/22./41
M7–16		43.58	0.75	13.73	0.07	14.51	0.30	12.52	13.77	0.75	0.03		60.6	2/32/0/28/36
103-C1	gl (5)	52.57 (28)	0.21 (10)	19.71 (62)	0.04 (6)	5.48 (14)	0.07 (8)	7.92 (48)	8.90 (40)	4.70 (32)	0.37 (10)	95.4 (26)	72.0 (11)	2/18/0/10./69
103-B1	gl (3)	51.62 (59)	0.17 (9)	17.99 (32)	0.16 (9)	6.43 (30)	0.11 (8)	9.79 (25)	10.42 (34)	3.16 (20)	0.16 (5)	96.1 (19)	73.1 (23)	0/16/8/14/62
103-A1[d]	gl (5)	51.4 (11)	0.14 (6)	15.05 (78)	0.25 (6)	6.04 (32)	0.13 (14)	12.72 (86)	12.61 (60)	1.63 (30)	0.04 (6)	97.7 (29)	79.0 (12)	0/8/21/23/48
	cpx (8)	54.01 (38)	0.05 (4)	4.40 (52)	0.82 (14)	3.53 (34)	0.10 (4)	22.2 (16)	14.6 (21)	0.27 (6)	<d.l	100.5 (5)	91.8 (2)	
	opx (8)	55.76 (62)	0.03 (4)	3.8 (13)	0.70 (20)	4.72 (24)	0.09 (4)	31.98 (76)	2.65 (22)	–	–	100.2 (3)	92.4 (2)	
	ol (5)	41.57 (22)	0.01 (4)	0.08 (2)	0.21 (6)	7.76 (20)	0.10 (2)	50.04 (40)	0.37 (6)	–	–	99.9 (3)	92.0 (1)	
103-D1	gl (14)	52.56 (60)	0.12 (4)	10.28 (58)	0.47 (6)	4.37 (88)	0.11 (10)	17.2 (11)	13.96 (48)	0.91 (32)	0.02 (4)	97.4 (10)	87.5 (27)	0/6/26./36/32
103-H2b	gl (7)	48.8 (83)	0.36 (11)	18.31 (41)	0.05 (9)	7.12 (31)	0.11 (10)	10.79 (27)	10.06 (38)	3.83 (22)	0.48 (9)	98.4 (11)	73.0 (5)	7/23/0/15/54
103-B2a	gl (8)	49.77 (72)	0.33 (4)	17.21 (42)	0.07 (6)	7.23 (22)	0.11 (4)	11.34 (32)	10.21 (38)	3.37 (14)	0.38 (6)	98.2 (20)	73.7 (8)	3/24/0/16/56
103-B2b	gl (9)	51.0 (16)	0.31 (6)	17.45 (48)	0.02 (6)	6.91 (36)	0.12 (6)	10.3 (11)	9.62 (56)	3.83 (28)	0.47 (14)	99.8 (2)	73.3 (16)	3/22/0/15/60
103-C2	gl (6)	49.4 (12)	0.27 (14)	17.0 (13)	0.09 (4)	7.48 (70)	0.06 (14)	12.6 (12)	10.16 (98)	2.74 (6)	0.19 (10)	96.1 (34)	75.0 (10)	0/27/1/14/58
103-E2	gl (3)	49.5 (12)	0.30 (2)	15.91 (32)	0.08 (0)	7.23 (2)	0.10 (2)	13.59 (62)	11.12 (8)	2.00 (76)	0.12 (2)	97.7 (22)	76.7 (7)	0/21/10/17/52
103-D2	gl (6)	50.0 (12)	0.21 (18)	13.47 (54)	0.20 (18)	7.29 (64)	0.15 (16)	14.60 (60)	12.28 (72)	1.80 (24)	0.08 (14)	100.1 (12)	78.1 (47)	0/20/9/26/44
103-F2	gl (8)	50.98 (36)	0.11 (4)	10.16 (24)	0.50 (6)	5.78 (20)	0.13 (10)	18.47 (30)	12.85 (34)	1.00 (12)	0.03 (6)	98.7 (11)	85.1 (6)	0/15/20/32/32
40-C1	gl (2)	48.03 (70)	1.65 (2)	16.6 (13)	0.04 (10)	13.20 (80)	0.25 (14)	7.18 (42)	8.2 (10)	4.49 (52)	0.40 (2)	96.2 (38)	49.2 (3)	7/24/0/14/52
40-D1	gl (8)	48.80 (54)	1.64 (32)	17.8 (19)	0.02 (10)	11.0 (29)	0.32 (16)	7.36 (146)	9.2 (13)	3.56 (90)	0.25 (16)	98.1 (21)	52.3 (66)	1/23/0/11/62
40-E1	gl (10)	49.36 (34)	0.80 (10)	18.87 (30)	0.03 (4)	9.40 (24)	0.13 (12)	7.98 (36)	9.99 (28)	3.23 (22)	0.21 (6)	98.9 (1)	60.2 (10)	0/22/1/11/65
40-B1n[d]	gl (5)	49.43 (80)	0.64 (8)	15.28 (76)	0.10 (4)	8.71 (42)	0.19 (12)	11.17 (48)	12.40 (66)	1.99 (14)	0.09 (8)	99.5 (12)	69.6 (9)	0/17/8/24/50
	cpx (7)	53.25 (40)	0.15 (8)	4.32 (62)	0.45 (6)	5.16 (54)	0.17 (8)	20.8 (11)	15.4 (17)	0.33 (6)	0.00 (2)	100.0 (7)	87.8 (5)	
	ol (13)	40.67 (20)	0.02 (4)	0.08 (2)	0.07 (4)	11.62 (14)	0.20 (6)	46.95 (20)	0.39 (8)	–	–	100.3 (4)	87.2 (1)	
40-A1[d]	gl (8)	49.76 (40)	0.61 (12)	14.91 (34)	0.11 (4)	8.31 (32)	0.19 (8)	11.58 (34)	12.47 (40)	1.98 (14)	0.08 (4)	99.0 (5)	71.3 (12)	0/16/9/25/49
	cpx (14)	53.46 (56)	0.18 (4)	3.91 (78)	0.31 (6)	5.08 (42)	0.18 (6)	21.15 (70)	15.43 (92)	0.30 (4)	0.01 (2)	99.9 (8)	88.1 (4)	
	ol (10)	40.41 (64)	0.02 (4)	0.07 (4)	0.11 (6)	11.48 (50)	0.20 (4)	47.30 (28)	0.41 (8)	–	–	100.5 (6)	88.0 (2)	
	sp (4)	0.32 (6)	0.42 (4)	61.75 (40)	0.53 (4)	23.51 (24)	0.18 (8)	13.07 (22)	0.22 (6)	0.01 (2)	0.00 (0)	99.1 (7)	49.8 (3)	
40-B1[d]	gl (13)	49.00 (34)	0.56 (10)	14.00 (18)	0.12 (8)	8.83 (22)	0.11 (10)	13.26 (26)	12.30 (56)	1.75 (12)	0.07 (2)	98.5 (9)	72.8 (3)	0/21/8/25/45
	ol (7)	40.91 (18)	0.01 (4)	0.06 (4)	0.10 (6)	9.70 (28)	0.19 (6)	48.70 (18)	0.33 (4)	–	–	100.1 (8)	91.1 (1)	
40-H2	gl (5)	52.66 (66)	1.09 (8)	20.19 (42)	0.02 (4)	7.51 (22)	0.13 (8)	4.29 (30)	5.73 (16)	6.74 (54)	1.63 (10)	95.1 (41)	50.5 (21)	12/14/0/7/65
40-F2	gl (28)	52.63 (52)	1.06 (8)	19.79 (32)	0.02 (6)	8.15 (26)	0.14 (8)	4.68 (20)	5.78 (30)	6.43 (32)	1.32 (14)	98.5 (12)	50.6 (15)	9/16/0/6/66
40-E2	gl (9)	50.62 (54)	1.08 (4)	19.67 (44)	0.00 (4)	10.01 (36)	0.15 (14)	5.78 (18)	6.74 (38)	5.40 (22)	0.53 (10)	98.0 (8)	50.7 (11)	6/21/0/5/66
40-A2	gl (2)	47.37 (48)	1.08 (24)	17.78 (34)	0.03 (0)	11.3 (14)	0.20 (10)	9.2 (10)	9.10 (30)	3.68 (12)	0.26 (4)	97.8 (15)	59.1 (56)	5/27/0/12/55
40-C2	gl (7)	48.21 (34)	0.93 (12)	16.77 (10)	0.01 (4)	11.53 (24)	0.30 (8)	9.38 (24)	9.33 (18)	3.37 (20)	0.16 (4)	99.2 (9)	60.1 (9)	2/27./0/13/56
40-B2	gl (7)	47.86 (34)	0.81 (12)	16.46 (36)	0.00 (6)	10.89 (44)	0.21 (10)	10.61 (18)	10.08 (8)	2.93 (16)	0.15 (6)	99.0 (13)	63.5 (8)	2/28/0/15/54
40-G2	gl (8)	48.49 (62)	0.65 (10)	14.62 (26)	0.10 (6)	9.34 (18)	0.20 (12)	12.89 (28)	11.66 (32)	1.96 (14)	0.10 (4)	99.6 (9)	71.1 (3)	0/24/5/22/48
40-D2a	gl (10)	48.82 (56)	0.52 (12)	12.77 (27)	0.13 (9)	8.50 (33)	0.19 (8)	15.65 (32)	11.72 (38)	1.62 (14)	0.07 (6)	99.0 (8)	76.64 (80)	0/25/8/25/42
16-F1	gl (7)	44.71 (36)	1.46 (8)	15.78 (22)	0.04 (4)	19.85 (26)	0.33 (10)	5.45 (18)	9.71 (44)	2.52 (22)	0.17 (4)	98.2 (10)	32.9 (8)	2/31/0/14/50
16-E1	gl (4)	44.04 (38)	1.33 (12)	15.32 (16)	0.01 (4)	18.40 (56)	0.37 (4)	7.43 (52)	11.58 (32)	1.46 (12)	0.08 (4)	98.8 (9)	41.8 (22)	0/31/0/20/48
16-B1	gl (8)	43.58 (62)	1.05 (8)	15.24 (34)	0.03 (6)	17.34 (54)	0.36 (6)	8.29 (56)	12.74 (28)	1.31 (22)	0.06 (4)	98.5 (12)	45.7 (19)	2/30/0/23/43
16-C1[d]	gl (8)	44.25 (40)	0.81 (8)	14.19 (28)	0.07 (8)	13.81 (36)	0.29 (6)	10.91 (24)	14.79 (40)	0.82 (16)	0.06 (4)	99.4 (13)	58.5 (10)	2/27/0/32/38
	ol (26)	39.56 (38)	0.01 (2)	0.09 (2)	0.06 (2)	16.85 (26)	0.29 (6)	42.41 (30)	0.59 (8)	–	–	100.1 (6)	81.8 (3)	
16-D2	gl (9)	42.43 (56)	2.28 (10)	13.68 (14)	0.01 (4)	23.23 (24)	0.37 (12)	5.55 (42)	8.49 (38)	2.83 (52)	1.13 (12)	97.6 (11)	29.9 (14)	9/33/0/18/36
16A2	gl (9)	41.55 (54)	1.59 (16)	14.63 (29)	0.01 (8)	21.78 (49)	0.36 (12)	7.48 (22)	9.81 (35)	2.46 (19)	0.32 (10)	99.0 (13)	37.98 (56)	8/36/0/18/35
16-B2	gl (6)	43.0 (11)	1.19 (14)	13.68 (92)	0.01 (6)	21.21 (86)	0.37 (24)	8.4 (18)	10.7 (11)	1.29 (74)	0.09 (12)	90.5 (38)	41.5 (52)	0/37/0/18/42
16-E2	gl (14)	42.86 (38)	1.18 (8)	13.67 (30)	0.03 (4)	19.94 (26)	0.36 (12)	9.13 (14)	11.58 (40)	1.22 (10)	0.05 (4)	99.0 (12)	44.9 (4)	2/35/0/22/40
16-C2	gl (10)	43.08 (32)	1.02 (8)	13.99 (24)	0.03 (6)	17.86 (32)	0.34 (6)	10.04 (18)	12.59 (30)	1.02 (10)	0.04 (6)	99.3 (10)	50.1 (7)	2/33/0/24/39

[a] Compositions of starting pyroxenites are given in lines 2 to 4, and phase compositions in partial melting experiments are given in the following lines (run numbers beginning with 103, 40, and 16 correspond to starting materials M5–103, M5–40, and M7–16, respectively). All compositions are normalized to a sum of 100% (the average original totals of electron probe analyses are reported in the column "Total"). Glass compositions were analysed in microdikes; the low analytical totals are due to beam overlap onto graphite. For a given phase in a given sample, we calculated the statistical dispersion of the dataset (as measured by 2σ, where σ is the standard deviation) and the analytical error (following Ancey et al., 1978), and we selected the largest of these two values as an estimation of the error. The errors (in parentheses) are given in terms of least unit cited: e.g., 52.57 (28) and 14.63 (206) represent 52.57 ± 0.28 and 14.63 ± 2.06, respectively. The number of analyses is given in parentheses in the second column.

[b] Mg# is the molar ratio 100 $Mg^{2+}/(Mg^{2+} + Fe^{2+})$; we considered that all iron was as Fe^{2+}.

[c] CIPW norms: nepheline (Ne)/olivine (Ol)/hypersthene (Hy)/diopside (Di)/anorthite + albite + orthose (Fds).

[d] Compositions of solid phases are given for 5 selected experiments (103-A1, 40-B1n, 40-A1, 40-B1 and 16 C1).

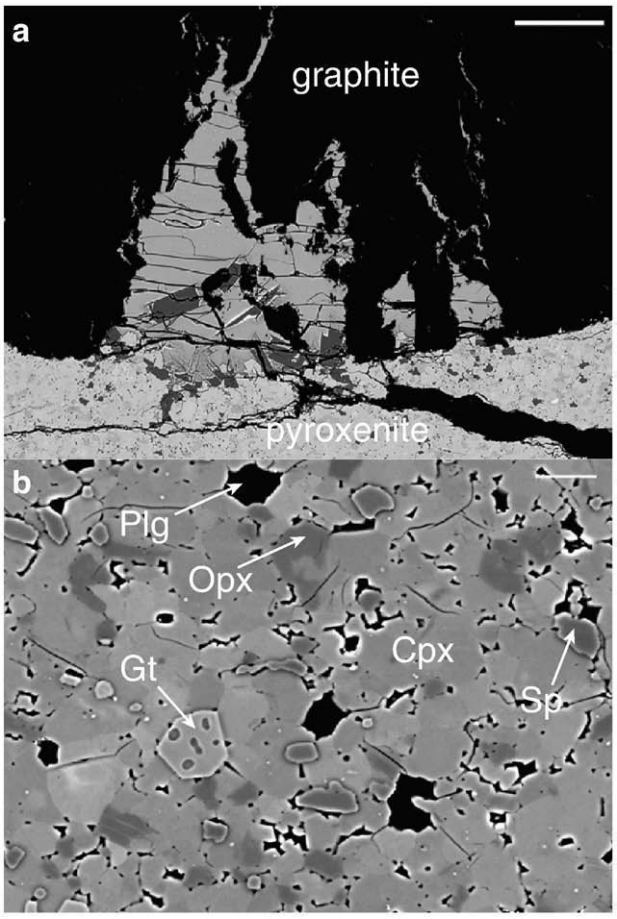

Fig. 2. Backscattered electron micrographs illustrating the melt extraction technique. (a) An overall view of the lower part of sample 40-F2, showing the graphite container (black), the partially molten pyroxenite (grey), and a basaltic microdike showing a large pool of glass. (b) Close-up view of the partially molten pyroxenite showing a small fraction of interstitial melt (3.4 wt.%) in equilibrium with Cpx, Opx, Plg, Sp and Gt. Scales: 100 μm in (a); 10 μm in (b).

beam current, counting times of 20 s for Ni, Cr and Ti, and of 10 s for other elements, and a focused beam were used for crystalline phases. For glass analyses, the beam current was lowered to 8 nA and a beam size of 5 μm was used whenever possible, otherwise 2 μm. Sodium loss was negligible, even for glass analyses with a 2 μm beam size (Laporte et al., 2004). In most cases, the analytical totals were good (98–100 wt.%), typical of basaltic glasses in nominally-anhydrous piston-cylinder experiments. Relatively low analytical totals (between 90 and 96 wt.%) were obtained in the case of very thin microdikes, due to beam overlap onto graphite. The proportions of liquid and solid phases best fitting the bulk composition of the starting material were calculated using a mass balance program modified from Albarède and Provost (1977).

3. Results

P–T conditions, run durations and phase proportions are summarized in Table 2. Melt compositions are reported in Table 1, as well as the compositions of mineral phases in selected experiments. Grain sizes in the run products range from 1 to 10 μm in subsolidus experiments up to ~150 μm near the liquidus. When present, Ol is homogeneous, both from core to rim of individual grains and throughout the capsule. In contrast, small relict cores are observed in some pyroxenes and garnets and reflect very low diffusional equilibration rates; microprobe analyses were carefully sorted to exclude residual core compositions. The low sums of squared residuals in mass balance calculations (Table 2) indicate that relict cores only represent a small fraction of the total of phase compositions and the bulk composition was preserved during the experiments. The differences between the values of the partition coefficients of Fe^{2+} and Mg between Ol and liquid measured in Ol-bearing experiments and those computed using the thermodynamical model of Toplis (2005) are lower than 0.02: according to Toplis (2005), such a good agreement implies that equilibrium was attained in our experiments. At last, we used the cpx-liquid thermometer of Putirka (2008a) in Cpx-bearing experiments as a test for equilibrium. The difference between the experimental temperature and the calculated one is 13.6 °C in average, with a range from 0.2 to 33 °C: this is well within the uncertainty of the geothermometer. Therefore, we can conclude that chemical equilibrium was closely approached owing to the long run durations (76 to 164 h; Table 2) and the fine grain size of starting materials.

3.1. Phase relations and melting reactions

3.1.1. Parageneses at or close to the solidus

In all cases, clinopyroxene [Cpx] is the major phase near the solidus, with proportions ranging from 49 to 84 wt.% (Table 2). The nature and abundance of the other solid phases (orthopyroxene [Opx], Ol, plagioclase [Plg], garnet [Gt], and spinel [Sp]) vary strongly with bulk composition and to a lesser extent with pressure. Opx is the second major phase after Cpx in the silica-rich composition M5–103, and in M5–40 at 1.5 GPa, whereas it is absent in the Ne-normative composition M7–16. At 1 GPa, Ol is present in the three compositions, with mass fractions ranging from 10 to 23%; at 1.5 GPa, it is less abundant than at 1 GPa, and even absent in M5–40. Plagioclase is present at 1 GPa in the three compositions, reaching 31% in M5–40; at 1.5 GPa, it is only present in M5–40. Garnet occurs in compositions M5–40 and M7–16 at 1.5 GPa. Spinel is present as traces in M5–103 at 1 and 1.5 GPa and in M5–40 at 1 GPa; it is more abundant in M5–40 at 1.5 GPa and in M7–16. Note that, unlike peridotites, pyroxenites with compositions close to M7–16 and M5–40 may contain the three aluminous phases, Plg, Sp and Gt, at equilibrium (Fig. 2b). The phase relations show that the proportions of Ol and Plg decrease with increasing pressure, whereas those of pyroxenes and Sp (±Gt) increase (Table 2). This is consistent with previous experiments in the CMAS system (Presnall et al., 1978).

3.1.2. Solidus and liquidus temperatures; melt productivities

The solidi of M5–103, M5–40 and M7–16 are ~1220 °C, ~1190 °C and ~1160 °C at 1 GPa and ~1270 °C, ~1190 °C and ~1230 °C at 1.5 GPa, respectively. The liquidus temperature was not reached in all our run series. It is higher than 1350 °C and 1450 °C for M5–103 at 1 and 1.5 GPa, respectively. The liquidus of M5–40 is close to 1320 °C at 1 GPa and to 1375 °C at 1.5 GPa, and that of M7–16 close to 1270 °C at 1 GPa and higher than 1310 °C at 1.5 GPa. The mean isobaric productivities are 0.5%/°C at 1 GPa and 0.3%/°C at 1.5 GPa for M5–103, 0.9%/°C at 1 GPa and 0.5–0.6%/°C at 1.5 GPa for M5–40, and 1%/°C at 1 GPa and 0.7%/°C at 1.5 GPa for M7–16. For comparison, the isobaric productivity of peridotites at 1 GPa is close to 0.2%/°C below the Cpx-out temperature (e.g., Baker and Stolper, 1994), and even lower after Cpx exhaustion. Overall, pyroxenites have lower solidus temperatures, higher melt productivities, and smaller melting intervals than peridotites (Fig. 3).

3.1.3. Melting reactions

The evolution of proportions of solid phases with increasing degree of melting allows to identify the main phases consumed and produced in the melting reaction. In detail, the melting reactions change from one composition to the other (Fig. 4) or as a function of pressure, but the general trend is as follows: (1) Plg and/or Gt are the first phases exhausted with increasing temperature; (2) after the disappearance of Plg and/or Gt, Opx (when present) is rapidly consumed in a reaction of

Table 2
A summary of run information: pressure, temperature, duration *t*, phase assemblages and modes.

Series	*P*	Run	*T*	*t*	Phases assemblages and modes (wt.%)[a]							∑r[b]
	(GPa)		(°C)	(h)	Cpx	Opx	Ol	Plg	Sp	Gt	Liquid	
M5–103	1	103-E1	1200	123	48.9 (36)	36.6 (53)	10.0 (32)	3.9 (15)	0.7 (4)	0	0	0.280
		103-C1	1230	140	53.2 (33)	34.8 (50)	7.2 (27)	0	0.1 (9)	0	4.6 (17)	0.473
		103-B1	1250	88	52.4 (36)	28.0 (49)	7.6 (24)	0	0	0	12.0 (18)	0.446
		103-A1	1290	86	39.5 (36)	16.8 (44)	12.6 (18)	0	0	0	31.1 (15)	0.303
		103-D1	1350	89	17.7 (46)	0	13.7 (28)	0	0	0	68.6 (29)	0.488
	1.5	103-H2a	1270	144	63.1 (40)	29.2 (55)	7.2 (24)	0	0.5 (4)	0	0	0.392
		103-H2b	1280	92	66.7 (50)	25.2 (60)	5.5 (24)	0	0	0	2.6 (14)	0.400
		103-B2a	1290	114	62.2 (37)	27.8 (45)	6.4 (19)	0	0	0	3.6 (13)	0.353
		103-B2b	1290	91	57.7 (40)	34.6 (56)	5.4 (28)	0	0	0	2.4 (18)	0.527
		103-C2	1330	164	60.5 (36)	27.0 (49)	5.7 (23)	0	0	0	6.8 (18)	0.473
		103-E2	1360	124	72.2 (78)	6.8 (90)	9.1 (34)	0	0	0	11.9 (27)	0.477
		103-D2	1390	92	60.2 (67)	5.0 (70)	6.2 (25)	0	0	0	28.6 (28)	0.251
		103-F2	1450	119	29.6 (20)	0	7.1 (10)	0	0	0	63.1 (12)	0.326
M5–40	1	40-F1	1175	96	46.4 (37)	0.0 (22)	22.7 (24)	30.9 (11)	0	0	0	0.315
		40-C1	1200	113	44.2 (21)	3.6 (35)	20.6 (23)	27.8 (17)	0	0	3.8 (13)	0.313
		40-D1	1225	101	44.1 (15)	2.1 (21)	19.6 (13)	23.0 (9)	0	0	11.2 (12)	0.207
		40-E1	1240	96	41.6 (32)	2.9 (43)	12.3 (33)	4.1 (32)	0.3 (7)	0	38.8 (28)	0.325
		40-B1n	1275	96	5.0 (11)	0	14.1 (4)	0	0	0	80.9 (9)	0.191
		40-A1	1290	76	0.6 (38)	0	14.4 (12)	0	0.4 (7)	0	84.6 (36)	0.392
		40-B1	1300	111	0	0	9.9 (5)	0	0	0	90.1 (9)	0.469
	1.5	40-H2	1200	139	71.3 (86)	14.1 (54)	0	3.8 (29)	4.1 (15)	3.1 (51)	3.0 (4)	0.245
		40-F2	1230	105	70.2 (66)	15.7 (41)	0	3.1 (24)	5.8 (19)	1.8 (68)	3.4 (10)	0.379
		40-E2	1250	97	72.7 (34)	11.2 (22)	0	0	2.7 (6)	0	13.5 (12)	0.444
		40-A2	1310	86	72.2 (26)	0.0 (30)	0	0	1.4 (6)	0	26.4 (24)	0.600
		40-C2	1310	89	67.8 (24)	0	0	0	2.0 (5)	0	30.2 (25)	0.518
		40-B2	1330	77	59.5 (32)	0	0	0	1.2 (9)	0	39.3 (31)	0.720
		40-G2	1360	105	12.9 (11)	0	8.0 (4)	0	0	0	79.1 (8)	0.212
		40-D2a	1375	81	0	0	3.1 (7)	0	0	0	96.9 (11)	0.535
		40-D2b	1375	121	0	0	0	0	0	0	100	
M7–16	1	16-D1	1165	119	68.5 (49)	0	12.9 (24)	11.8 (32)	6.6 (12)	0	0	0.616
		16-F1	1185	102	73.3 (6)	0	4.6 (3)	0	7.7 (2)	0	14.4 (6)	0.187
		16-E1	1225	90	47.0 (9)	0	6.9 (4)	0	4.8 (3)	0	41.4 (10)	0.225
		16-B1	1250	115	37.2 (9)	0	6.2 (3)	0	4.0 (2)	0	52.7 (10)	0.197
		16-C1	1265	98	0	0	5.0 (5)	0	0	0	95.0 (9)	0.456
		16-A1	1290	83	0	0	0	0	0	0	100	
	1.5	16-D2	1230	125	84.2 (8)	0	2.6 (2)	0	8.6 (3)	1.8 (12)	2.9 (2)	0.138
		16-A2	1250	126	80.5 (10)	0	2.6 (5)	0	7.3 (4)	0	9.4 (9)	0.253
		16-B2	1270	149	59.6 (7)	0	2.1 (3)	0	6.2 (2)	0	32.2 (8)	0.165
		16-E2	1290	100	49.8 (3)	0	2.6 (1)	0	4.9 (1)	0	42.8 (30)	0.229
		16-C2	1310	103	33.9 (11)	0	3.1 (3)	0	3.5 (2)	0	59.5 (11)	0.093

[a] Modes are calculated using a mass balance program modified from Albarède and Provost (1977). The numbers in parentheses are 2σ standard deviations, given in terms of the least unit cited: e.g., 48.9 (36) and 0.7 (4) represent 48.9 ± 3.6 and 0.7 ± 0.4, respectively.
[b] $\sum r^2$ is the sum of the squared residuals using the modes obtained from the mass balance program.

the form Cpx + Opx ± Sp = liquid + Ol; (3) after the disappearance of Opx (at 50% maximum of melting), Cpx becomes the main contributor to melt production, in a reaction of the form Cpx ± Sp = liquid + Ol; and (4) Ol is generally consumed with Plg at low *F* but, after Plg exhaustion, it is on the product side on the Opx- and Cpx-consuming melting reactions in all series. As a result, Ol is the liquidus phase for the three compositions at both pressures (Fig. 4).

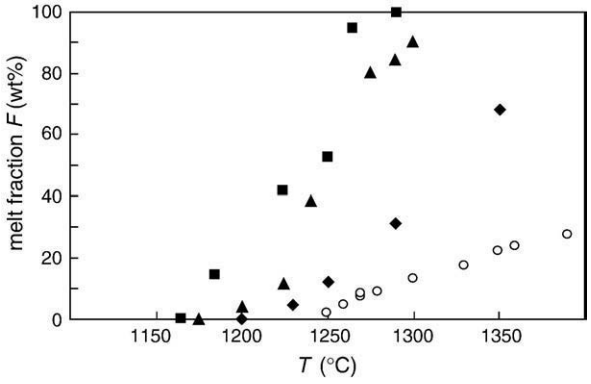

Fig. 3. Temperature–melt fraction curves for pyroxenites M5–103 (*diamonds*), M5–40 (*triangles*) and M7–16 (*squares*) at 1 GPa; the data for fertile lherzolite MM3 (*circles*; Baker and Stolper, 1994; Baker et al., 1995) are shown for comparison. The uncertainties on melt percentages (1σ) are smaller than symbols.

Contrasted melting behaviors are observed depending on the presence or absence of Opx at the solidus. If Opx is abundant, such as in the Ol websterite M5–103, the main melting reaction is similar to the melting reaction in peridotites: for instance, 0.61 Cpx + 0.49 Opx = 1 liquid + 0.10 Ol in M5–103 at 1 GPa (as Ol is a product, this reaction may also hold in the case of Ol-free websterites) vs. 0.71 Cpx + 0.38 Opx + 0.13 Sp = 1 liquid + 0.22 Ol in fertile lherzolite MM3 (Baker and Stolper, 1994). Accordingly, the chemical trends of melts from websterites should mimic those of peridotitic melts despite major differences in the modal fractions of solid phases, as discussed below. The main difference is that Opx disappears before Cpx in websterites such as M5–103, yielding a wherlitic residue, whereas Cpx disappears first in peridotites. For the Opx-free pyroxenite M7–16, the main melting reaction at 1 GPa (after Plg exhaustion) is 0.95 Cpx + 0.10 Sp = 1 liquid + 0.05 Ol, and should give liquids strongly depleted in SiO_2 in comparison to liquids produced by Opx-bearing rock types.

3.2. Melt compositions

Oxide concentrations in melts are plotted as a function of *F* in Fig. 5. The evolutionary trends often show slope breaks or even

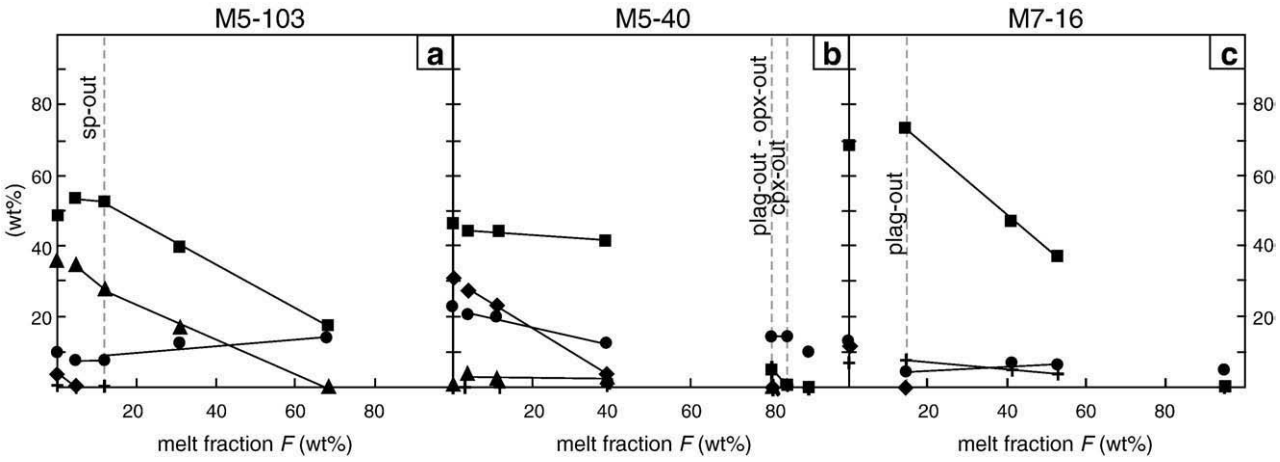

Fig. 4. Fractions (wt.%) of solid phases vs. melt fraction *F* for pyroxenites (a) M5–103, (b) M5–40, and (c) M7–16 at 1 GPa. The straight lines are the best fit lines used to compute the coefficients of the melting reactions. Symbols are as follows: *squares* for Cpx, *triangles* for Opx, *circles* for Ol, *diamonds* for Plg and *crosses* for Sp. The uncertainties on phase percentages are given in Table 2.

reversals that reflect exhaustion of a solid phase and change in the melting reaction. There is a distinct "source effect" for some oxides: their concentration in melts varies strongly from one pyroxenite to another in direct relation to variations in bulk composition. The main aspects of the evolution of melt compositions may be summarized as follows:

(1) MgO increases with *F*, ranging from 4–5% in M5–40 and M7–16 at low *F* to 18.5% in M5–103 at high *F*.
(2) FeO shows contrasted behaviors as a function of bulk composition, from large FeO contents that decrease continuously in FeO-rich composition M7–16, to low and nearly constant contents in FeO-poor composition M5–103. The combination of high FeO and low MgO leads to very low Mg# in M7–16 melts: from 30 at low *F* to 59 at high *F*, as compared to 49–77 in M5–40 melts and 72–88 in M5–103 melts (Table 1).
(3) SiO_2 varies little in a given pyroxenite at a given pressure, but strongly from one pyroxenite to the other: in particular, the liquids produced in silica-poor composition M7–16 are strongly depleted in SiO_2 (41.6–44.7%) in comparison to those produced in silica-rich composition M5–103 (48.8–52.6%). These contrasted SiO_2 contents are due to the fact that the major contributors to melt production are Opx + Cpx in M5–103 (Fig. 4a) vs. Cpx + Sp in M7–16 (Fig. 4c).
(4) Al_2O_3 behaves as a typical incompatible element in M5–103 at 1 and 1.5 GPa, and in M5–40 at 1.5 GPa, decreasing from 18–20% to ~10% in M5–103 and 13% in M5–40 with increasing *F*. In M5–40 at 1 GPa, Al_2O_3 first increases during melting due to the large coefficient of Plg in the melting reaction (Fig. 4), then it decreases after the exhaustion of Plg. Al_2O_3 content in liquids from M7–16 varies little with *F* (from 15.8 to 14.2% at 1 GPa, and from 14.6 to 13.7% at 1.5 GPa); this behavior is presumably due to the high mode of Sp (Table 2), which makes Al_2O_3 less incompatible in the residual assemblage and buffers the alumina content in the liquid at a high level.
(5) CaO systematically increases with increasing *F* until the disappearance of Cpx at high degrees of melting (stage that is only attained in M5–40).
(6) TiO_2, Na_2O, and K_2O behave as typical incompatible elements, with concentrations increasing with decreasing *F*. The Na_2O contents of near-solidus M5–103 liquids are higher at 1 GPa than at 1.5 GPa, indicating a slight decrease of Na incompatibility with increasing pressure; indeed, the bulk partition coefficient of Na_2O increases from 0.08 at 1 GPa to 0.12 at 1.5 GPa. In M5–40 at 1 GPa, Plg is abundant and Na_2O becomes truly incompatible only after Plg exhaustion, at melt fractions exceeding 40%.

4. Discussion

To explore the effects of source heterogeneity on MORB compositions, we considered a heterogeneous mantle made of pyroxenites (M5–103, M5–40, and M7–16 compositions) and peridotites, undergoing adiabatic decompression melting. For the peridotite end-member, we choose a series of fertile and depleted compositions previously used for experimental melting (see the caption of Fig. 6 for references). The difference of melting properties (solidus temperatures and melt productivities) of peridotites and pyroxenites renders difficult to model adiabatic decompression melting of such a heterogeneous mantle. For instance, assuming thermal equilibrium, the earlier melting of pyroxenites leads to delayed melting of peridotites (compared to pure peridotite mantle; e.g., Hirschmann and Stolper, 1996). In the same way, beginning of melting of more refractory domains (such as peridotites) may result in a decreased melt productivity in more fertile domains (such as pyroxenites; e.g., Phipps Morgan, 2001). In the following discussion, we assumed that pyroxenites and peridotites behave as closed systems until melt extraction, and we neglected thermal interactions between them during decompression melting. Two cases are discussed:

(1) We suppose that pyroxenite-derived melts may be sampled directly, without experiencing interactions with neighboring peridotites or mixing with peridotite-derived melts. We can thus compare the melt compositions in our experiments with partial melts from peridotites from the literature to determine the major-element signature of pyroxenite-derived melts. The comparison is made at 1 GPa and temperatures of 1245 °C to 1305 °C. This is the range of temperatures expected at 1 GPa in a mantle undergoing adiabatic decompression melting, assuming a range of potential temperatures (T_P) from 1280 to 1400 °C and using the parameterization of McKenzie and Bickle (1988) and McKenzie and O'Nions (1991). This range of T_P was recently proposed by Herzberg et al. (2003) on the basis of new estimates of the parental magma compositions of MORB. It is consistent with the range proposed by Klein and Langmuir (1987) and Langmuir et al. (1992) for most MORB (1300–1400 °C), but competing models favor an ambient mantle temperature uniformly low ($T_P \approx 1260$ °C; Shen and Forsyth, 1995; Presnall et al., 2002), uniformly high ($T_P \approx 1400$ °C in Putirka, 2008b; $T_P \approx 1430$ °C in Green et al., 2001), or a range of

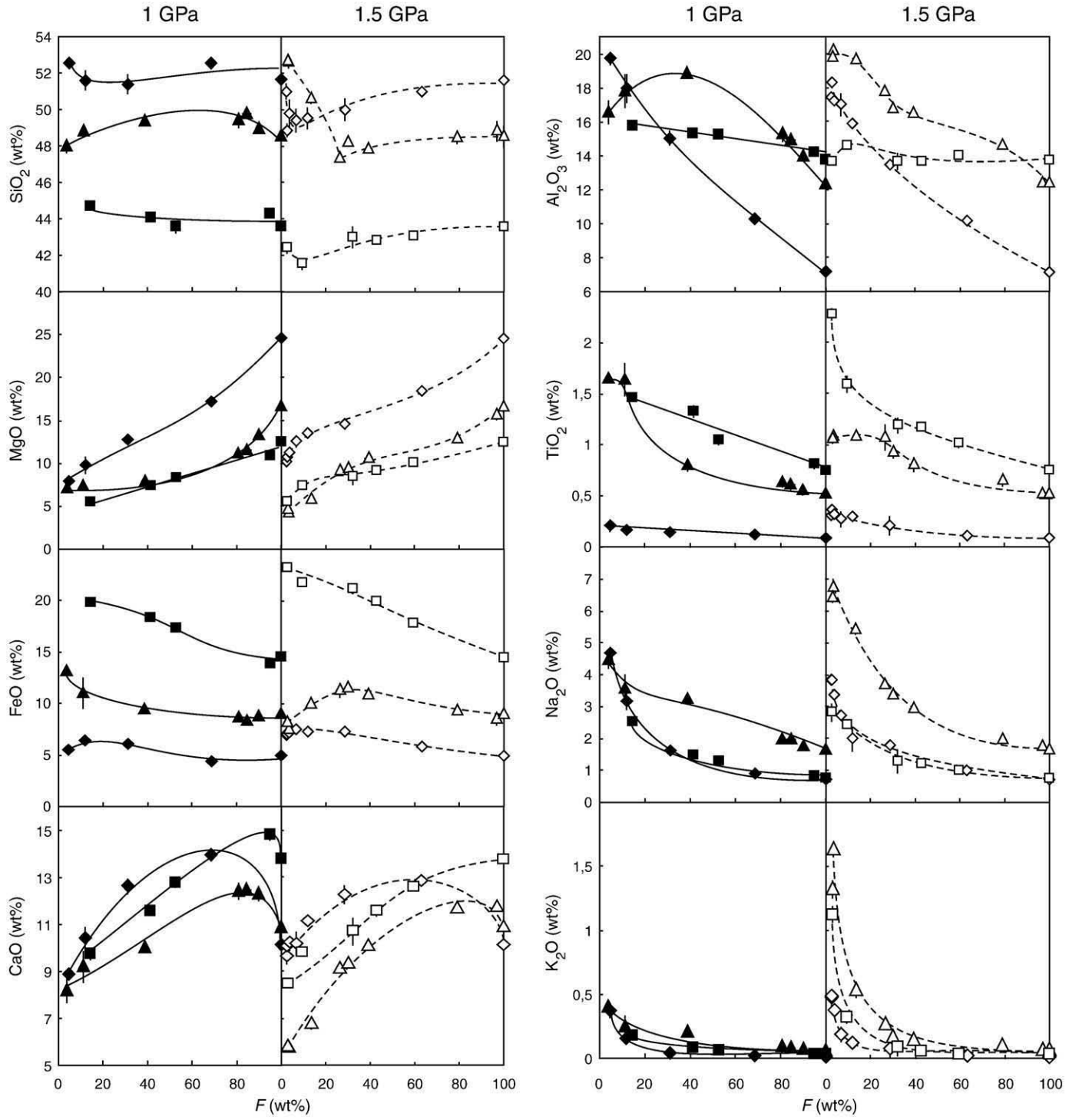

Fig. 5. Oxide concentrations in melts plotted as a function of melt fractions *F*. Symbols are as follows: *diamonds* for pyroxenite M5–103, *triangles* for M5–40, and *squares* for M7–16; the closed symbols are for the experiments at 1 GPa, the open symbols for the ones at 1.5 GPa. The data plotted at $F = 100\%$ correspond to the bulk-rock composition. When not visible, the error bar (1σ) is smaller than the symbol.

temperatures with a high mean value ($T_P \approx 1450 \pm 85$ °C; Putirka et al., 2007).

(2) We consider that pyroxenite- and peridotite-derived melts are mixed somewhere between their source region and the ridge, and we compute the average melt composition as a function of the proportion of pyroxenite in the mantle and the compositions of peridotite and pyroxenite. Despite its simplifications, this scenario provides an insight into the impact of source heterogeneity on the major-element composition of MORB.

4.1. Pyroxenite- vs. peridotite-derived melts: looking for discrimination features

The compositions of partial melts of pyroxenites and peridotites at 1 GPa are plotted as a function of temperature in Fig. 6. Despite the major chemical and lithological contrasts between pyroxenites and peridotites, these two rock types yield liquids with widely overlapping major-element compositions, especially in the temperature range of interest (1245–1305 °C; Fig. 6). In particular, SiO_2, Al_2O_3, CaO,

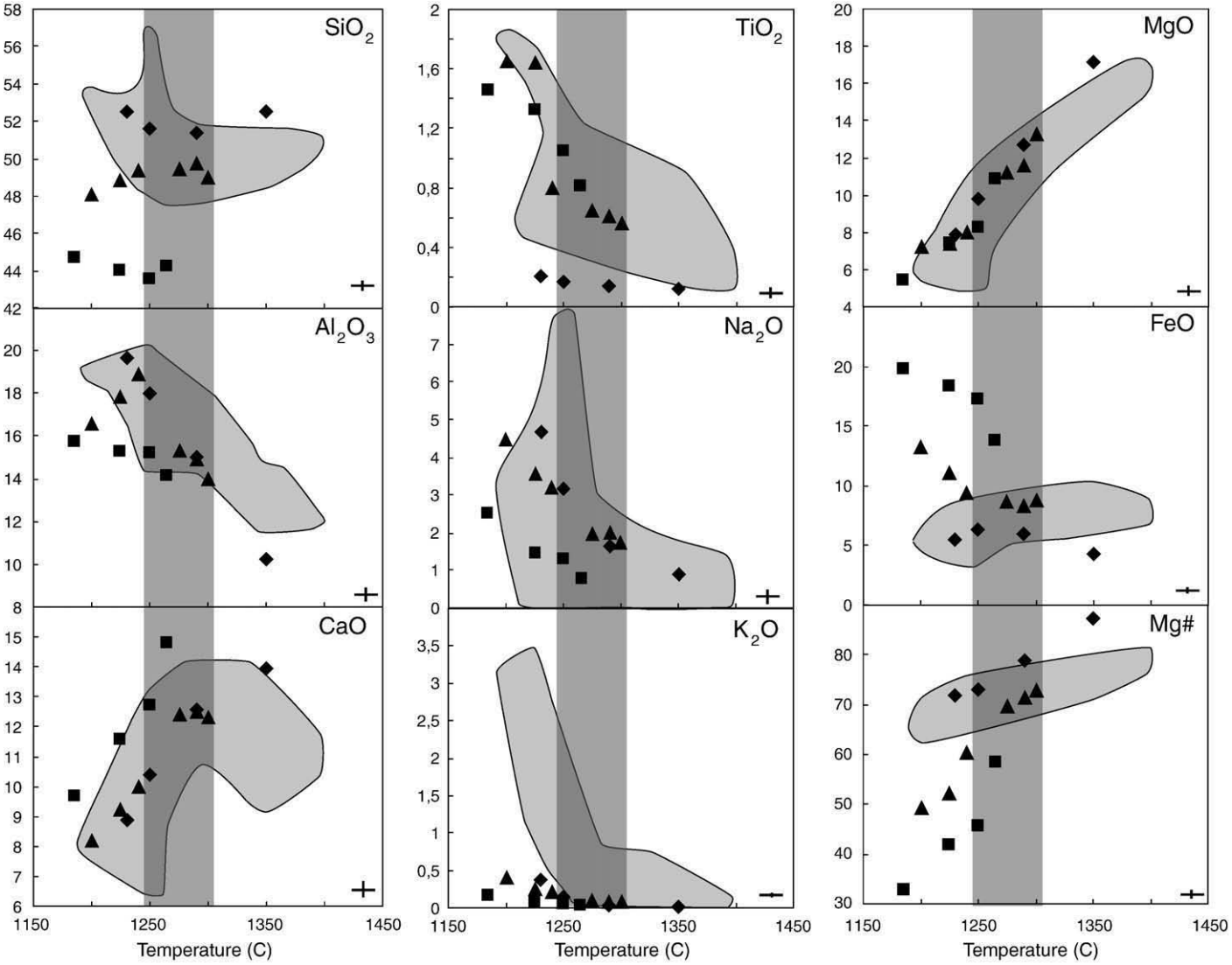

Fig. 6. Average melt compositions in pyroxenites M5–103, M5–40, and M7–16 at 1 GPa plotted as a function of temperature. The temperature interval of 1245–1305 °C represented by shaded boxes corresponds to the range of temperatures (at 1 GPa) of a mantle undergoing adiabatic decompression melting (assuming potential temperatures in the range 1280–1400 °C, McKenzie and Bickle (1988)). Symbols are as follows: *diamonds*, M5–103; *triangles*, M5–40; *squares*, M7–16. Grey fields correspond to liquids produced by peridotites PHN1611 (Kushiro, 1996), MM3 (Baker and Stolper, 1994; Baker et al., 1995; Hirschmann et al., 1998), DMM1 (Wasylenki et al., 2003) and Depma (Laporte et al., 2004). Error bars (1σ on oxide concentrations; ± 5 °C on temperature) are shown in the bottom right corner of each diagram.

MgO, FeO, and Na_2O in liquids from Ol websterite M5–103 fall in the field of peridotitic melts at all degrees of melting except the highest; the same is true for liquids from websterite M5–40 at moderate to high degrees of melting. Some data plot, however, distinctly out of the field of peridotites: for instance, SiO_2 and FeO in M7–16, TiO_2 in M5–103, etc. As a matter of fact, some major elements have been considered in the past as markers of a heterogeneous mantle source for MORB. They include alkali oxides and TiO_2, which behave as incompatible elements (e.g., Niu et al., 1999, 2002), but also FeO (Shen and Forsyth, 1995). On the basis of our experimental data, we can evaluate the reliability of these markers in the context of mid-ocean ridges.

4.1.1. Alkali oxides and TiO_2

Pyroxenites contain 2 to 75 times more Na_2O than peridotites. However, partial melts from pyroxenites and peridotites have very similar Na_2O contents (Fig. 6), suggesting that Na_2O cannot be used to discriminate pyroxenite melts from peridotite melts. This result finds its explanation in two properties of pyroxenites. Firstly, at a given *P* and *T*, pyroxenites are expected to undergo much larger degrees of partial melting than peridotites (Fig. 3). Accordingly, pyroxenite and peridotite may yield liquids with similar Na_2O concentrations despite the higher Na_2O concentration of the former. Secondly, Na_2O is less incompatible in pyroxenites than in peridotites because of the higher proportion of Cpx in pyroxenites. This results in an enrichment factor (the Na_2O content in the partial melt divided by the bulk Na_2O content) lower in pyroxenites (at most 6.6 in our experiments) than in peridotites (for instance, from 10 to 40 in depleted peridotite DMM1; Wasylenki et al., 2003). The same reasoning can be done about K_2O. The much larger degrees of melting achieved in pyroxenites (and, to a lesser extent, the abundance of Plg, which makes potassium slightly less incompatible in pyroxenites than in peridotites) lead to the counterintuitive result that pyroxenite-derived melts are poorer in K_2O than peridotite-derived melts (Fig. 6).

TiO_2 behaves as a mildly incompatible element during partial melting. Natural pyroxenites show a wide range of TiO_2 contents, from $\leq 0.1\%$ to 2–3%, as compared to 0.1–0.3% in fertile peridotites. For pyroxenites with intermediate TiO_2 contents (such as M5–40 and M7–16), the large degrees of melting reached at 1 GPa and 1245–1305 °C yield liquids with TiO_2 contents indistinguishable from those

of peridotite-derived melts. Ti-poor pyroxenite M5–103 produced, however, partial melts depleted in TiO_2 compared to peridotite-derived melts (Fig. 6), and we anticipate that partial melts enriched in TiO_2 may be produced in the case of pyroxenites with 2–3% TiO_2.

4.1.2. FeO contents and Mg# of pyroxenite-derived liquids

The trends of MgO content as a function of temperature for melts from pyroxenites and peridotites are almost perfectly superimposed (Fig. 6). On the contrary, the behavior of FeO, and therefore of Mg#, differs markedly between the two rock types, with many pyroxenite-derived liquids having much higher FeO contents and lower Mg#'s than peridotite-derived melts. This result is illustrated in Fig. 7 where the liquid-Mg# is plotted as a function of mass fraction of melt *F*. Liquid-Mg# increases linearly with *F*, reaching the bulk-Mg# at $F=1$.

$$\text{Liquid} - \text{Mg\#} = a(F-1) + \text{bulk} - \text{Mg\#} \quad (1)$$

The slope *a* is strongly correlated with the bulk-Mg#, decreasing from 31.9 in M7–16 (Mg# = 60.6), to 26.9 in M5–40 (Mg# = 76.7), to 19.8 in M5–103 (Mg# = 89.8), and to 16.0 in peridotite MM3 (Mg# = 90.5; Baker and Stolper, 1994). Therefore, for a given melt fraction interval, the variations of liquid-Mg# in pyroxenite-derived melts may be up to twice larger than in peridotite-derived melts. The small variation of the FeO content in peridotite-derived melts at a given *P* is well documented in lherzolite melting experiment (e.g., Kinzler and Grove, 1992; Baker and Stolper, 1994; Kushiro, 1996; Gudfinnsson and Presnall, 2000) and is due to the olivine buffering effect. Indeed, because the olivine composition in an olivine-rich system remains nearly unchanged with increasing degree of melting, the Mg# of the melt evolves within a narrow range (Médard et al., 2006). Hence, while the FeO content of melt from peridotites evolves within a narrow band at a given *P* (≈4 to 10%; Fig. 6), our three pyroxenites produce liquids with FeO contents ranging from 4.4 wt.% to 19.9 wt.%. Pyroxenites such as M7–16 are of special interest because

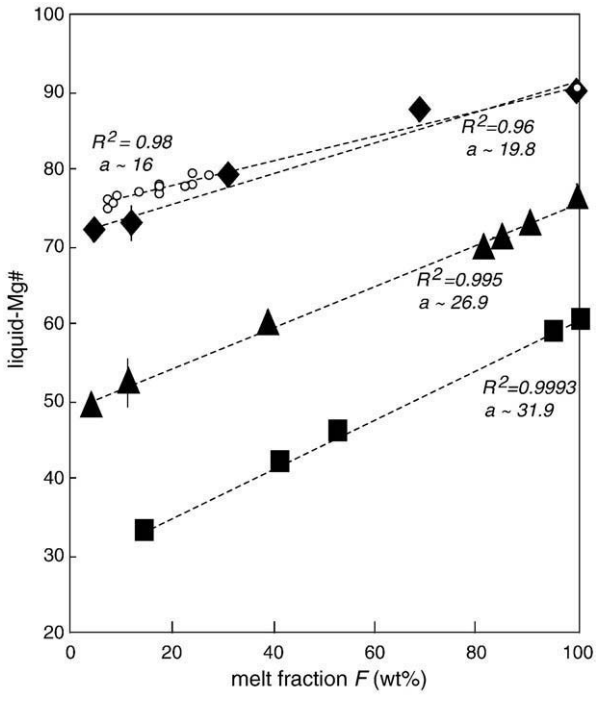

Fig. 7. Liquid-Mg# vs. melt fraction in pyroxenites M5–103, M5–40, and M7–16 at 1 GPa and in peridotite MM3 (Baker and Stolper, 1994). For each composition, the regression line is shown by the dashed line, and the correlation coefficient R^2 and the slope *a* are given. Symbols are as follows: *diamonds*, M5–103; *triangles*, M5–40; *squares*, M7–16; *empty circles*, MM3. When not visible, the error bar (1σ) is smaller than the symbol.

of their relatively low bulk-Mg#: even at high degrees of melting, they yield liquids strongly enriched in FeO, with Mg#'s clearly out of the range of peridotite-derived melts. Such pyroxenites are not exceptions as compositions with a bulk-Mg# lower than 65 makes about 30% of natural pyroxenites (Fig. 1a).

4.1.3. SiO_2 as a tracer of pyroxenite-derived melts

Silica content is usually considered as a pressure indicator in basalt genesis (Klein and Langmuir, 1987). Indeed, the silica content of peridotite-derived melts increases with decreasing pressure, due to the expansion of the liquidus phase volume of Ol at the expense of pyroxenes. In the case of a heterogeneous mantle, our experiments show, however, that liquids with very different SiO_2 contents may be produced at a single pressure (Fig. 6): Opx-bearing pyroxenites M5–40 and M5–103 yield liquids with SiO_2 contents ($51 \pm 3\%$) in the range of peridotite-derived melts, whereas the Opx-free clinopyroxenite M7–16 produces liquids strongly depleted in SiO_2 (≈44% at 1 GPa). In fact, the silica content in partial melt is well correlated with the bulk silica content (51.6, 48.5, and 43.6% in M5–103, M5–40, and M7–16, respectively) in all our experiments, with a ratio (SiO_2 in liquid)/(bulk SiO_2) always close to unity. About 43% of natural pyroxenites have a bulk SiO_2 in the range $45 \pm 3\%$ (Fig. 1b); however, they may not all produce SiO_2-poor liquids as melt compositions are controlled by modal composition and melting reaction. Primary basalts with low silica contents may be produced if the melting region contains a significant proportion of low-SiO_2 clinopyroxenites.

4.1.4. Summary

Although most pyroxenites produce melts with major-element compositions that are hardly distinguishable from peridotite-derived melts (Fig. 6), some pyroxenites yield melts with an identifiable signature, such as a low-SiO_2 content, a high FeO content (and a low Mg#), a low K_2O content or a low TiO_2 content. Interestingly, pyroxenites with low-SiO_2 and high FeO contents define a distinct end-member in the compositional cloud of natural pyroxenites (Fig. 1b).

The basis for the comparison shown in Fig. 6 is that pyroxenites evolve as closed systems and are equilibrated at the same *P–T* conditions as neighboring peridotites, implying thus that melt extraction from pyroxenites would only proceed at high degrees of melting. The entrapment of pyroxenite-derived melts into their parent body is conceivable before the onset of melting of surrounding peridotites, but not after, when the system is in a regime closer to polybaric near-fractional melting (e.g., Johnson et al., 1990; Langmuir et al., 1992). We stress, however, that our main conclusions are not sensitive to the exact timing of melt extraction, as the SiO_2 and the FeO signals would even be stronger in the case of melt extraction from pyroxenites at low to moderate degrees of melting (Fig. 6). This is even more true if the extraction occurs at high pressure as, at a given *F* and within the range of melting pressures beneath mid-ocean ridges, the FeO content of pyroxenite-derived melts is expected to increase and their SiO_2 content to decrease with increasing pressure (e.g., Hirschmann et al., 2003), as in peridotite-derived melts (e.g., Klein and Langmuir, 1987).

4.2. The contribution of pyroxenite-derived melts to basalt generation at mid ocean ridges

On the basis on their proportion in orogenic peridotite massifs, pyroxenites might constitute 2–5% of the upper mantle (Hirschmann and Stolper, 1996) and even more in hotspot-influenced regions of the convecting mantle (Spray, 1989). However, using isotopic considerations, Pertermann and Hirschmann (2003a) estimated that the abundance of pyroxenites in MORB mantle sources might be lower (<1–2%) than previously anticipated. As pyroxenites have higher melt productivities than peridotites, the proportion of pyroxenite melts in MORB must be higher than the proportion of pyroxenites in their

sources: the enrichment factor (i.e., the proportion of melt derived from pyroxenites divided by the proportion of pyroxenites in the source) would vary from 3–4 (Hirschmann and Stolper, 1996) to 10 (Pertermann and Hirschmann, 2003a).

Current models of dynamic melting at mid-ocean ridges have shown that MORB are mixes of melts from all depths in the melting column (e.g., McKenzie and O'Nions, 1991; Langmuir et al., 1992). Let us consider a heterogeneous mantle made of a minor pyroxenitic component into a host peridotite; the mass fraction of pyroxenites in the heterogeneous source is Π_S. The mass fraction of pyroxenite-derived liquid in the average liquid, Π_L, is given by:

$$\Pi_L = (\Pi_S \times F_{Py}) / [(\Pi_S \times F_{Py}) + (1-\Pi_S) \times F_{Pe}] \quad (2)$$

where F_{Py} and F_{Pe} are the mean degrees of melting in pyroxenites and in peridotites, respectively. For a normal crust thickness (7 ± 1 km), the mean pressure of melting is <1.5 GPa (e.g., Langmuir et al., 1992; Kinzler and Grove, 1992) and the mean degree of melting is 9–14% (Kinzler and Grove, 1992; Kinzler, 1997). Using the experimental data on peridotite MM3 by Baker and Stolper (1994) and our data on pyroxenites, we can compute Π_L and the composition of the average liquid as a function of the composition and mass fraction Π_S of pyroxenites in the source. We chose a mean pressure of melting equal to 1 GPa, and a temperature of 1275 °C; these *P–T* conditions correspond to a potential temperature of 1325 °C beneath mid-ocean ridges (McKenzie and O'Nions, 1991). Our aim is not to simulate melting of a heterogeneous mantle at a spreading center (as previously underlined, this would need a sophisticated model of decompression melting), but rather to discuss the parameters that are likely to influence the relative contribution of pyroxenite-derived melts to basalt generation.

4.2.1. Effect of pyroxenite composition on Π_L

We first made a set of calculations with a heterogeneous mantle made of 98 wt.% MM3 and 2 wt.% ($\Pi_S = 0.02$) of M5–103, M5–40, or M7–16 to evaluate the effect of pyroxenite composition on Π_L. At 1 GPa and 1275 °C, the degree of melting F_{Py} in pyroxenites ranges from 26.3% in M5–103, to 80.4% in M5–40, and to 100% in M7–16 (Fig. 3), and the degree of melting F_{Pe} in lherzolite MM3 is equal to 7.8%. We computed the fraction of pyroxenite-derived liquids in the average liquid using Eq. (2): Π_L is small (0.064) for M5–103 due to its small degree of melting, and much larger for M5–40 and M7–16 ($\Pi_L = 0.174$ and 0.207, respectively) due to their large degrees of melting. As the fraction of pyroxenites in the source is small, the degree of melting averaged over the whole mantle is only slightly sensitive to the choice of pyroxenite composition: 8.2% for M5–103, 9.3% for M5–40, and 9.6% for M7–16.

4.2.2. Effect of Π_S on Π_L

We first consider a heterogeneous mantle made of lherzolite MM3 and a fraction of pyroxenite M5–40 ranging from 1 to 8%. In this case, the fraction of pyroxenite-derived liquids increases rapidly with increasing Π_S: from 0.09 at $\Pi_S = 0.01$ to 0.473 at $\Pi_S = 0.08$. More generally, if the upper mantle contains 2–5% of pyroxenites, the average liquid may contain from ~6% of pyroxenite melts (for 2% pyroxenites with a low melt productivity, such as M5–103) up to 35–40% (for 5% pyroxenites with high melt productivities, such as M5–40 and M7–16); in the latter case, the enrichment factor may reach very high values: $\Pi_L/\Pi_S \approx 7$–8. Our values of Π_L are close to that reported by Sobolev et al. (2007) who used olivine phenocryst compositions in basalt to estimate the contribution of pyroxenite-derived melts in MORB (10–30%). If Π_S approaches 10% as it does locally in the Beni Bousera ultramafic massif (Pearson and Nixon, 1996), then the contribution of pyroxenites to the total melt production may exceed the contribution of peridotites. Several authors used a fixed value of the enhancement factor to estimate the fraction of pyroxenites into mantle sources from isotopic and trace element compositions of basalts (e.g., Le Roux et al., 2002; Pertermann and Hirschmann, 2003a). The ratio Π_L/Π_S is, however, very variable as a function of the compositions and the relative abundances of peridotites and pyroxenites, and the use of a constant ratio may lead to biased estimates of Π_S.

4.2.3. Composition of average liquids

To evaluate the effect of the abundance and composition of a pyroxenitic component on the composition of average melts, we considered a peridotitic mantle (of type MM3) that contains 0 to 8% of pyroxenite M5–103, M5–40, or M7–16. At 1 GPa and 1275 °C, the average degree of melting of such a heterogeneous mantle ranges from 7.8% (for pure MM3) to 15.2% (for 8% of M7–16), in good agreement with the values (9-14%, Kinzler and Grove, 1992; Kinzler, 1997) expected for a normal oceanic crust. For a given value of Π_S and for a given pyroxenite, we "mixed" a fraction Π_L of pyroxenite-derived liquid and a fraction $(1-\Pi_L)$ of MM3-derived liquid to obtain the composition of the average liquid. Composition of partial melt in MM3 at 1 GPa–1275 °C is interpolated from the data of Baker and Stolper (1994), Baker et al. (1995) and Hirschmann et al. (1998). The FeO and SiO_2 contents in the average melts are compared to those in MM3 partial melt in Fig. 8. As emphasized above, partial melts from pyroxenites M5–103 and M5–40 have SiO_2 contents (51.5 and 49.4%, respectively) and FeO contents (6.2 and 8.7%, respectively) close to peridotite melts ($SiO_2 = 50.4\%$ and FeO = 6.0% in MM3 at $F_{Pe} = 7.8\%$). Accordingly, addition of even a high fraction of these two pyroxenites has only a marginal effect on the SiO_2 and FeO contents of the average

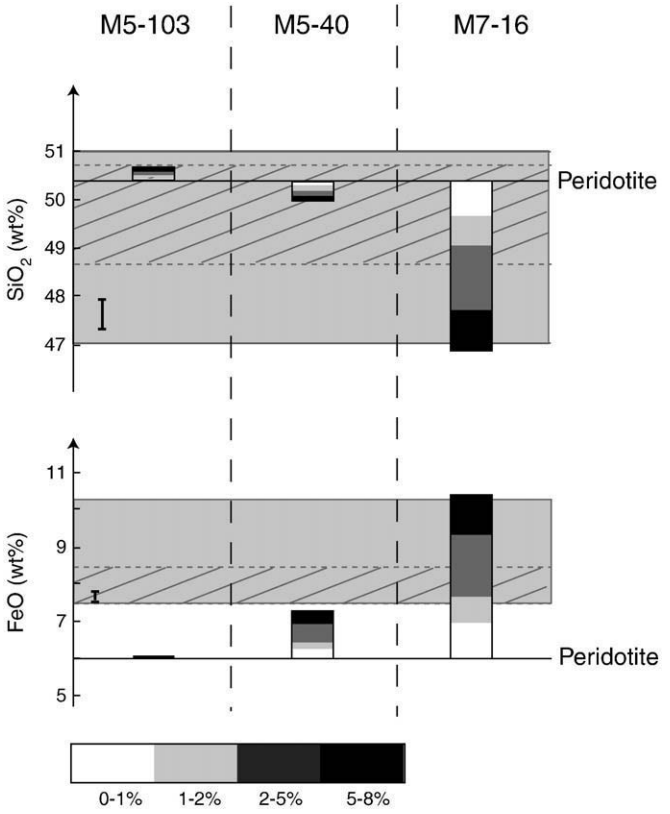

Fig. 8. SiO_2 and FeO contents in melt produced by peridotite MM3 at 1275 °C and 1 GPa (solid line; Baker and Stolper, 1994), and in the average melt of a heterogeneous mantle made of peridotite MM3 and 1 to 8% of pyroxenite M5–103, M5–40, or M7–16. The ranges of SiO_2 and FeO in MORBs with either MgO ≥9 wt.% (grey boxes) or Mg# ≥67 (hatched boxes) are shown for comparison. MORB data sources: Smithsonian Institution catalogue (Melson and O'Hearn, 2003: http://www.petdb.org/petdbWeb/index.jsp).

melt (Fig. 8; the same conclusion holds for MgO, CaO, and Al_2O_3). On the contrary, addition of pyroxenite M7–16, which yields melts strongly depleted in SiO_2 (43.6%) and enriched in FeO (14.5%), may change significantly the average melt composition: with the addition of 5% of M7–16 in the source, the SiO_2 content of the average melt decreases from 50.8 to 47.9%, and the FeO content increases from 6.0 to 9.4%.

4.2.4. Comparison with primitive MORB

Mid-Ocean Ridge Basalts with the highest Mg#'s are often considered as the most primitive, and therefore the closest to primary liquids (e.g., Mg# ≥68 in Presnall et al., 2002). The range of SiO_2, and FeO in MORB with Mg# ≥67 is shown in Fig. 8: 48.7 to 50.7% for SiO_2, and 7.5 to 8.5% for FeO. As discussed above, the presence of pyroxenites in mantle sources can strongly affect the FeO content of average liquids (Fig. 8), without changing their MgO content (Fig. 6), thus leading to primary compositions with anomalously low Mg#'s: selecting primitive MORB on the basis of a high Mg# eliminates such primary compositions. To circumvent this difficulty, we decided to make a second selection based on a MgO content ≥9%: the range of silica contents mainly extends toward lower values (down to 47%) and the range of iron contents extends toward much higher values (up to 10.3%). In Melson and O'Hearn's database (2003), 15% of MORB with a MgO content ≥9% have both a FeO content higher than 8.5 wt.% (and a Mg# <67) and a SiO_2 content lower than 48.7 wt.%. Accordingly, there are distinct compositions of primitive MORB with high MgO (but Mg# <67), relatively low SiO_2, and relatively high FeO. These compositions are presumably not related to low-pressure fractionation as this process tends to increase the silica content of melts (Grove et al., 1992). The lower SiO_2 contents and the higher FeO contents are consistent with an increase of the average depth of melting (Klein and Langmuir, 1987; Langmuir et al., 1992), but not the lower Mg#'s as the Mg# of primary basalts is expected to increase with increasing pressure (Ulmer, 1989). Such compositions are therefore good candidates to be primitive MORB carrying a pyroxenite signature (of the type imparted by clinopyroxenites such as M7–16; Fig. 8) and, as such, deserve careful attention.

4.2.5. On the loss of the pyroxenite signal en route to the ridge

A major unknown is how well the chemical signature of pyroxenite-derived liquids can survive the interactions with neighboring peridotites during their transport to the surface. The answer is probably not unique as it will depend on many parameters, such as the size of pyroxenitic bodies in the heterogeneous mantle (Kogiso et al., 2004) and the transport mechanism (pervasive porous flow, focused flow in dunite channels, or magma transport in dikes). We can, however, distinguish two cases:

(1) In many instances and for most major elements, pyroxenite-derived melts are similar to peridotite-derived melts (Fig. 6). They thus probably suffer minor interactions with the overlying peridotitic mantle and are likely to preserve their chemical signatures. This provides one possible explanation for an important result of the melt inclusion studies, namely the observation that primitive melt inclusions within a single phenocryst or a single lava sample have relatively uniform major-element compositions, but their trace element patterns may be highly variable (see Schiano, 2003, and references therein). It is generally believed that such a large range of trace-element abundances is due to a chemical disequilibrium between the host phase and all trapped melts, which thus may have their initial melt compositions modified by post-entrapment diffusion processes. An alternative hypothesis is that the inclusions isolate instantaneous compositions of primitive pyroxenite- and peridotite-derived melts in equilibrium with the host phase.

(2) Some pyroxenites produce melts that are strongly out of equilibrium with mantle peridotites. For instance, M7–16 melts are too poor in silica to be in equilibrium with Opx, and have a too low Mg# to be in equilibrium with a peridotite with a bulk Mg# equal to ≈90. If magma migration occurs by pervasive porous flow, these liquids will react with overlying peridotites and dissolve pyroxene (e.g., Daines and Kohlstedt, 1994), so that their composition will approach that of peridotite-derived melt. Conversely, if magma moves by focused flow in dunite channels, then M7–16 melts and their analogues may preserve part of their specific signature because they all have Ol as the liquidus phase. In the case of M7–16, the liquidus Ol has a low Mg# (≈82; Table 1) compared to Ol in dunite channels (≈91; Kelemen et al., 1995). Accordingly, the liquid will equilibrate with the surrounding dunite and lose its low Mg# signature (partly or totally depending on the magma/rock ratio) whereas its low-SiO_2 signature should remain unchanged. Finally, both the low Mg# signature and the low-SiO_2 signature may be preserved if pyroxenite-derived liquids are transported in dikes, but such a mechanism would presumably require that pyroxenites form large isolated bodies into the heterogeneous mantle.

The persistence of a major-element signature distinctive of pyroxenite-derived melts up to the ridge seems plausible, at least in some instances. However, if this signature includes a low Mg-number, it may get lost “in the laboratory” due to the use of inappropriate criteria to select primary magmas. Let us assume, for example, that the melt from run 16-C1 is directly transported to the surface: it has a bulk Mg# of 58.5 and is in equilibrium with an Ol with Mg# = 81.8 (Table 1), so it will not pass the usual tests made to identify primitive magmas in MORB studies (a bulk Mg# close to 70) and in melt inclusion studies (a host Ol with high Mg#). It has, however, a high MgO content (10.9%), which may be the only criterion to recognize its primary nature.

5. Conclusions

Using the 1–1.5 GPa phase relations and the melt compositions of two websterites and one clinopyroxenite representative of worldwide pyroxenite variability, we have compared the compositions of pyroxenite- and peridotite-derived melts in order to investigate the role of pyroxenites in basalt generation at mid-ocean ridges. The key results of our study are as follows:

(1) Contrasted melting behaviors are observed depending on the abundance of Opx at the solidus. If Opx is abundant, such as in the Ol websterite M5–103, the main melting reaction is similar to the melting reaction in peridotites (Cpx + Opx ± Sp = liquid + Ol), and the chemical trends of melts mimic those of peridotitic melts. In the absence of Opx, the main melting reaction is Cpx + Sp = liquid + Ol, yielding liquids that are strongly depleted in SiO_2 in comparison to liquids produced by websterites and peridotites.
(2) Many pyroxenites produce liquids that are similar to peridotite-derived melts for most major elements (SiO_2, Al_2O_3, CaO, MgO, and FeO). This may explain why MORB have relatively uniform major-element compositions, but may have variable trace element and isotopic compositions.
(3) Due to the larger degrees of melting of pyroxenites at given P and T, their melts are not enriched (and may even be depleted) in incompatible elements (alkali oxides and TiO_2) in comparison to peridotite-derived melts. Therefore, the concentrations of these elements cannot be used as markers of pyroxenites in MORB mantle sources.
(4) Some pyroxenites yield melts with a distinct signature, such as a low-SiO_2 content and/or a high FeO content, two features usually ascribed to a high average pressure of melting (of a peridotitic source).

(5) Because of their higher melt productivities and lower solidus temperatures, 5% of pyroxenites in the source region may contribute up to 40% of the total melt production.
(6) Partial melting of a heterogeneous mantle may produce primary liquids with anomalously low Mg# ($\leq$60). The usual tests that are made to select primitive magmas (melt inclusions hosted into high Mg# Ol or MORB glasses with a Mg# $\geq$67) will eliminate these anomalous compositions.

Acknowledgments

The authors are grateful to Prof. Jacques Kornprobst for providing the three pyroxenites from Beni Bousera used in this study. This study has benefited from discussions with Sébastien Pilet, Etienne Médard and Marion Le Voyer. Special thanks are due to the following persons: Jean-Louis Fruquière and Franck Pointud for manufacturing the piston-cylinder assemblages and for maintenance operations; Jean-Luc Devidal and Jean-Marc Hénot for technical assistance with the electron microprobe and the scanning electron microscope; Ariel Provost for his mass-balance program; Mhammed Benbakkar for the ICP-AES analysis of the starting materials in Table 1. Keith Putirka and Marc M. Hirschmann are gratefully acknowledged for their constructive reviews. This study was supported by the program DyETI of the Institut National des Sciences de l'Univers (INSU-CNRS), through grants to D. Laporte.

References

Adam, J., Green, T.H., Day, R.A., 1992. An experimental study of two garnet pyroxenite xenoliths from the Bullenmerri and Gnotuk Maars of western Victoria, Australia. Contrib. Mineral. Petrol. 111, 505–514.
Albarède, F., Provost, A., 1977. Petrological and geochemical mass-balance equations: an algorithm for least-square fitting and general error analysis. Comput. Geosci. 3, 309–326.
Allègre, C.J., Turcotte, D.L., 1986. Implications of a two-component marble-cake mantle. Nature 323, 123–127.
Allègre, C.J., Schiano, P., Lewin, E., 1995. Differences between oceanic basalts by multitrace element ratio topology. Earth Planet. Sci. Lett. 129, 1–12.
Ancey, M., Bastenaire, F., Tixier, R., 1978. Application des méthodes statistiques en microanalyse. In: Maurice, F., Meny, L., Tixier, R. (Eds.), Microanalyse, microscopie à balayage. Les éditions du Physicien, Orsay, pp. 323–347.
Baker, M.B., Stolper, E.M., 1994. Determining the composition of high-pressure mantle melts using diamond aggregates. Geochim. Cosmochim. Acta 58, 2811–2827.
Baker, M.B., Hirschmann, M.M., Ghiorso, M.S., Stolper, E.M., 1995. Compositions of near-solidus peridotite melts from experiments and thermodynamic calculations. Nature 375, 308–311.
Becker, H., 1996. Crustal trace element and isotopic signatures in garnet pyroxenites from garnet peridotite massifs from lower Austria. J. Petrol. 37, 785–810.
Blichert-Toft, J., Albarède, F., Kornprobst, J., 1999. Lu–Hf isotope systematics of garnet pyroxenites from Beni Bousera, Morocco: implications for basalt origin. Science 283, 1303–1306.
Bodinier, J.-L., Garrido, C.J., Chanefo, I., Bruguier, O., Gervilla, F., 2008. Origin of pyroxenite–peridotite veined mantle by refertilization reactions: evidence from the Ronda Peridotite (Southern Spain). J. Petrol. 49, 999–1025.
Daines, M.J., Kohlstedt, D.L., 1994. The transition from porous to channelized flow due to melt/rock reaction during melt migration. Geophy. Res. Lett. 21, 145–148.
Dessai, A.G., Markwick, A., Vaselli, O., Downes, H., 2004. Granulite and pyroxenite xenoliths from the Deccan Trap: insight into the nature and composition of the lower lithosphere beneath cratonic India. Lithos 78, 263–290.
Dickey, J.S., 1970. Partial fusion products in alpine-type peridotites: Serrania de la Ronda and other examples. Miner. Soc. Am. Spec. Pap. 3, 33–49.
Ducea, M.N., 2002. Constraints on the bulk composition and root foundering rates of continental arcs: a California arc perspective. J Geophys. Res. 107 (B11), 2304. doi:10.1029/2001JB000643.
Dupré, B., Allègre, C.J., 1983. Pb–Sr isotope variation in Indian Ocean Basalts and mixing phenomena. Nature 303, 142–146.
Eiler, J.M., Schiano, P., Kitchen, N., Stolper, E.M., 2000. Oxygen-isotope evidence for recycled crust in the sources of mid-ocean-ridge basalts. Nature 403, 530–534.
Falloon, T.J., Danyushevsky, L.V., 2000. Melting of refractory mantle at 1.5, 2 and 2.5 GPa under anhydrous and H_2O-undersaturated conditions: implications for the petrogenesis of high-Ca boninites and the influence of subduction components on mantle melting. J. Petrol. 41, 257–283.
Garrido, C.J., Bodinier, J.-L., 1999. Diversity of mafic rocks in the Ronda peridotite: evidence for persuasive melt–rock reaction during heating of subcontinental lithosphere by upwelling asthenosphere. J. Petrol. 40, 729–754.
Ghent, E.D., Coleman, R.G., Hadely, D.G., 1980. Ultramafic inclusions and host alkali olivine basalts of the southern coastal plain of the Red Sea, Saudi Arabia. Am. J. Sci. 280, 499–527.
Green, D.H., Falloon, T.J., Eggins, S.M., Yaxley, G.M., 2001. Primary magmas and mantle temperatures. Eur. J. Mineral. 13, 437–451.
Grove, T.L., Kinzler, R.J., Bryan, W.B., 1992. Fractionation of Mid-Ocean Ridge Basalt (MORB). Geophys. Monogr. 71, 281–310.
Gudfinnsson, G.H., Presnall, D.C., 2000. Melting Behaviour of Model Lherzolite in the System CaO-MgO-$Al2O_3$-SiO_2-FeO at 0.7-GPa–2.8 GPa. J. Petrol. 41, 1241–1269.
Herzberg, C., Asimow, P.D., Arndr, N., Niu, Y., Lesher, C.M., Fitton, J.G., Cheadle, M.J., Saunders, A.D., 2003. Temperature in ambient mantle and plumes: constraints from basalts, picrites and komatiites. Geochem. Geophys. Geosyst. 8. doi:10.1029/2006GC001390.
Hirose, K., Kushiro, I., 1993. Partial melting of dry peridotites at high pressures: determination of compositions of melts segregated from peridotite using aggregates of diamond. Earth Planet. Sci. Lett. 114, 477–489.
Hirschmann, M.M., Stolper, E.M., 1996. A possible role for garnet pyroxenite in the origin of the "garnet signature" in MORB. Contrib. Mineral. Petrol. 124, 185–208.
Hirschmann, M.M., Baker, M.B., Stolper, E.M., 1998. The effects of alkalis on the silica content of mantle-derived melts. Geochim. Cosmochim. Acta 62, 883–902.
Hirschmann, M.M., Kogiso, T., Baker, M.B., Stolper, E.M., 2003. Alkalic magmas generated by partial melting of garnet pyroxenite. Geology 31, 481–484.
Ito, K., Kennedy, G.C., 1974. The composition of liquids formed by partial melting of eclogites at high temperatures and pressures. J. Geol. 82, 383–392.
Jahn, B., Fan, Q., Yang, J.-J., Henin, O., 2003. Petrogenesis of the Maowu pyroxenite–eclogite body from the UHP metamorphic terrane of Dabieshan: chemical and isotopic constraints. Lithos 70, 243–267.
Johnson, K.T., Dick, H.J.B., Schimizu, N., 1990. Melting in the oceanic upper mantle: an ion microprobe study of diopsides in abyssal peridotites. J. Geophys. Res. 95, 2661–2678.
Kelemen, P.B., Shimizu, N., Salters, V.J.M., 1995. Extraction of Mid-Ocean Ridge Basalt from the upwelling mantle by focused flow of melt in dunite channels. Nature 375, 747–753.
Keshav, S., Gudfinnsson, G.H., Sen, G., Fei, Y., 2004. High-pressure melting experiments on garnet clinopyroxenite and the alkalic to tholeiitic transition in ocean-island basalts. Earth Planet. Sci. Lett. 223, 365–379.
Kinzler, R.J., 1997. Melting of a mantle peridotite at pressures approaching the spinel to garnet transition: applications to Mid-Ocean Ridge Basalt petrogenesis. J. Geophys. Res. 102, 853–874.
Kinzler, R.J., Grove, T.L., 1992. Primary magmas of Mid-Ocean Ridge Basalts 2. Applications. J. Geophys. Res. 97, 6907–6926.
Klein, E.M., Langmuir, C.H., 1987. Global correlations of ocean ridge basalt chemistry with axial depth and crustal thickness. J. Geophys. Res. 92, 8089–8115.
Kogiso, T., Hirschmann, M.M., 2006. Partial melting experiments of bimineralic eclogite and the role of recycled mafic oceanic crust in the genesis of ocean island basalts. Earth Planet. Sci. Lett. 249, 188–199.
Kogiso, T., Hirose, K., Takahashi, E., 1998. Melting experiments on homogeneous mixtures of peridotite and basalt: application to the genesis of ocean island basalts. Earth Planet. Sci. Lett. 162, 45–61.
Kogiso, T., Hirschmann, M.M., Reiners, P.W., 2004. Length scales of mantle heterogeneities and their relationship to ocean island basalt geochemistry. Geochim. Cosmochim. Acta 68, 345–360.
Kornprobst, J., 1970. Les péridotites et les pyroxenolites du massif ultrabasique des Beni Bouchera: une etude experimentale entre 1100 et 1550 C sous 15 a 30 kilobars de pression seche. Contrib. Mineral. Petrol. 29, 290–309.
Kumar, N., Reisberg, L., Zindler, A., 1996. A major and trace element and strontium, neodymium, and osmium isotopic study of a thick pyroxenite layer from the Beni Bousera ultramafic complex of northern Morocco. Geochim. Cosmochim. Acta 60, 1429–1444.
Kuno, H., Aoki, K.-I., 1970. Chemistry of ultramafic nodules and their bearing on the origin of basaltic magmas. Phys. Earth Planet. Int. 3, 273–301.
Kushiro, I., 1996. Partial melting of a fertile mantle peridotite at high pressures: an experimental study using aggregates of diamond. In: Basu, A., Hart, S. (Eds.), Earth Processes: Reading the Isotopic Code: Geophysical Monogaph, vol. 95, p. 437.
Lambart, S., Laporte, D., Schiano, P., 2009. An experimental study of focused magma transport and basalt–peridotite interactions beneath mid-ocean ridges: implications for the generation of primitive MORB composition. Contrib. Mineral. Petrol. 157, 429–451.
Langmuir, C.H., Klein, E.M., Plank, T., 1992. Petrological systematics of mid-ocean ridge basalts: constraints on melt generation beneath ocean ridges. Am. Geophys. Union Monogr. 71, 183–280.
Laporte, D., Toplis, M., Seyler, M., Devidal, J.-L., 2004. A new experimental technique for extracting liquids from peridotite at very low degrees of melting: application to partial melting of depleted peridotite. Contrib. Mineral. Petrol. 146, 463–484.
Le Roux, P.J., Le Roex, A.P., Schilling, J.G., 2002. MORB melting processes beneath the southern mid-Atlantic ridge (40–55 degrees S): a role for mantle plume-derived pyroxenite. Contrib. Mineral. Petrol. 144, 206–229.
Lee, C.-T.A., Cheng, X., Horodyskyj, U., 2006. The development and refinement of continental arcs by primary basaltic magmatism, garnet pyroxenite accumulation, basaltic recharge and delamination: insights from the Sierra Nevada, California. Contrib. Mineral. Petrol. 151, 22–242.
Liu, Y., Gao, S., Lee, C.-T.A., Hu, S., Liu, X., Yuan, H., 2005. Melt–peridotite interactions: links between garnet pyroxenite and high-Mg# signature of continental crust. Earth Planet. Sci. Lett. 234, 39–57.
McKenzie, D., Bickle, M.J., 1988. The volume and composition of melt generated by extension of the lithosphere. J. Petrol. 29, 625–679.
McKenzie, D., O'Nions, R.K., 1991. Partial melt distributions from inversion of rare earth element concentrations. J. Petrol. 32, 1021–1091.
Médard, E., Schmidt, M.W., Schiano, P., Ottolini, L., 2006. Melting of amphibole-bearing wehrlites: an experimental study on the origin of ultra-calcic nepheline-normative melts. J. Petrol. 47, 491–504.
Melcher, F., Meisel, T., Puhl, J., Koller, F., 2002. Petrogenesis and geotectonic setting of ultramafic rocks in the Eastern Alps: constraints from geochemistry. Lithos 65, 69–112.

Melson, W.G., O'Hearn, T., 2003. Smithsonian Volcanic Glass File. PetDB database (http://petdb.ldeo.columbia.edu).
Michael, P.J., 1995. Regionally distinctives sources of depleted MORB: evidence from trace elements and H_2O. Earth Planet. Sci. Lett. 131, 301–320.
Michael, P.J., Schilling, J.-G., 1989. Chlorine in mid-ocean ridge magmas: evidence for assimilation of seawater-influenced components. Geochim. Cosmochim. Acta 53, 3131–3143.
Niu, Y., Batiza, R., 1997. Trace element evidence from seamounts for recycled oceanic crust in the Eastern Pacific mantle. Earth Planet. Sci. Lett. 148, 471–483.
Niu, Y., Collerson, K.D., Batiza, R., Wendt, I.J., Regelous, M., 1999. Origin of enriched-type Mid-Ocean Ridge Basalt at ridges far from mantle plumes: The East Pacific Rise at 11°20′N. J. Geophys. Res. 104, 7067–7087.
Niu, Y., Regelous, M., Wendt, I.J., Batiza, R., O'Hara, M.J., 2002. Geochemistry of near-EPR seamounts: importance of source vs. process and the origin of enriched mantle component. Earth Planet. Sci. Lett. 199, 327–345.
Pearson, D.G., Nixon, P.H., 1996. Diamonds in young orogenic belts: graphitised diamonds from Beni Bousera, N. Morocoo, a comparison with kimberlite-derived diamond occurences and implications for diamond genesis and exploration. Afr. Geosci. Rev. 3, 295–316.
Pertermann, M., Hirschmann, M.M., 2003a. Partial melting experiments on a MORB-like pyroxenite between 2 and 3 GPa: constraints on the presence of pyroxenite in basalt source regions from solidus location and melting rate. J. Geophys. Res. 108 (B2), 2125. doi:10.1029/2000JB000118.
Pertermann, M., Hirschmann, M.M., 2003b. Anhydrous partial melting experiments on a MORB-like eclogite: phase relations, phase compositions and mineral-melt partitioning of major elemens at 2–3 GPa. J. Petrol. 44, 2173–2201.
Phipps Morgan, J., 2001. Thermodynamics of pressure release melting of a veined plum pudding mantle. Geochem. Geophys. Geosyst. 2. doi:10.1029/2000GC000049.
Porreca, C., Selverstone, J., Samuels, K., 2006. Pyroxenite xenoliths from the Rio Puerco volcanic field, New Mexico: melt metasomatism at the margin of the Rio Grande rift. Geosphere 2, 333–351.
Presnall, D.C., Dixon, S.A., Dixon, J.R., O'Donnell, T.H., Brenner, N.L., Schrock, R.L., Dycus, D.W., 1978. Liquidus phase relations on the join diopside–forsterite–anorthite at 1 atm to 20 kbar; their bearing on the generation and crystallization of basaltic magma. Contrib. Mineral. Petrol. 66, 203–220.
Presnall, D.C., Gudfinnson, G.H., Walter, M.J., 2002. Generation of Mid-Ocean Ridge Basalts at pressure from 1 to 7 GPa. Geochim. Cosmochim. Acta 66, 2073–2090.
Putirka, K.D., 2008a. Thermometers and barometers for volcanic systems. Rev. Mineral. Geochem. 69, 61–120.
Putirka, K.D., 2008b. Excess temperatures at ocean islands: implications for mantle layering and convection. Geology 36, 283–286.
Putirka, K.D., Perfit, M., Ryerson, F.J., Jackson, M.G., 2007. Ambient and excess mantle temperatures, olivine thermometry, and active vs. passive upwelling. Chem. Geol. 241, 177–206.
Robinson, J.A.C., Wood, B.J., Blundy, J.D., 1998. The beginning of melting of fertile and depleted peridotite at 1.5 GPa. Earth Planet. Sci. Lett. 155, 97–111.
Santos, J.F., Schärer, U., Gil Ibarguchui, J.I., Girardeau, J., 2002. Genesis of pyroxenite-rich peridotite at Cabo Ortegal (NW Spain): geochemical and Pb–Sr–Nd isotope data. J. Petrol. 43, 17–43.
Schiano, P., 2003. Primitive mantle magmas recorded as silicate melt inclusions in igneous minerals. Earth-Sci. Rev. 63, 121–144.
Schmickler, B., Jacob, D.E., Foley, S.F., 2004. Eclogite xenoliths from the Kuruman kimberlites, South Africa: geochemical fingerprinting of deep subduction and cumulate processes. Lithos 75, 173–207.
Schulze, D.J., 1989. Constraints on the abundance of eclogite in the upper mantle. J. Geophys. Res. 94 (B4), 4205–4212.
Shen, Y., Forsyth, D.W., 1995. Geochemical constraints on initial and final depths of melting beneath mid-ocean ridges. J. Geophys. Res. 100 (B2), 2211–2237.
Sleep, N.H., 1984. Tapping of magmas from ubiquitous mantle heterogeneities: an alternative to mantle plumes. J. Geophys. Res. 89, 10029–10041.
Sobolev, A.V., Hofmann, A.W., Kuzmin, D.V., Yaxley, G.M., Arndt, N.T., Chung, S.-L., Danyushevsky, L.V., Elliott, T., Frey, F.A., Garcia, M.O., Gurenko, A.A., Kamenetsky, V.S., Kerr, A.C., Krivolutskaya, N.A., Matvienkov, V.V., Nikogosian, I.K., Rocholl, A., Sigurdsson, I.A., Sushchevskaya, N.M., Teklay, M., 2007. The amount of recycled crust in sources of mantle-derived melts. Science 316, 412–417.
Spray, J.G., 1989. Upper mantle segregation processes: evidence from alpine-type peridotite. In: Saunders, A.D., Norry, M.J. (Eds.), Magmatism in the ocean basins: Geol Soc Spec Publ, vol. 42, pp. 29–40.
Tang, H.-F., Liu, C.-Q., Nakai, S., Orihashi, Y., 2007. Geochemistry of eclogites from the Dabie–Sulu terrane, eastern China: new insights into protoliths and trace element behaviour during UHP metamorphism. Lithos 95, 441–457.
Toplis, M.J., 2005. The thermodynamics of iron and magnesium partitioning between olivine and liquid: criteria for assessing and predicting equilibrium in natural and experimental systems. Contrib. Mineral. Petrol. 149, 22–39.
Ulmer, P., 1989. The dependence of the Fe^{2+}–Mg cation partitioning between olivine and basaltic liquid on pressure, temperature and composition. Contrib. Mineral. Petrol. 101, 261–273.
Volkova, N.I., Frenkel, A.E., Budanov, V.I., Lepezin, G.G., 2004. Geochemical signatures for eclogite protolith from the Maksyutov Complex, South Urals. J. Asian Earth Sci. 23, 745–749.
Wasylenki, L.E., Baker, M.B., Kent, A.J.R., Stolper, E.M., 2003. Near-solidus melting of the shallow upper mantle: partial melting experiments on depleted peridotite. J. Petrol. 44, 1163–1191.
Xu, Y., 2002. Evidence for crustal components in the mantle and constraints on crustal recycling mechanisms: pyroxenite xenoliths from Hannuoba, North China. Chem. Geol. 182, 301–322.
Yasuda, A., Fujii, T., Kurita, K., 1994. Melting phase relations of an anhydrous Mid-Ocean Ridge Basalt from 3 to 20 GPa: implications for the behavior of subducted oceanic crust in the mantle. J. Geophys. Res. 99 (B5), 9401–9414.